nature cell biology

Article

https://doi.org/10.1038/s41556-024-01422-x

Mapping putative enhancers in mouse oocytes and early embryos reveals TCF3/12 as key folliculogenesis regulators

Received: 17 January 2023

Accepted: 11 April 2024

Published online: 5 June 2024



Bofeng Liu^{1,2,8}, Yuanlin He^{3,4,8}, Xiaotong Wu^{2,5,8}, Zili Lin^{1,2,8}, Jing Ma^{1,2,8}, Yuexin Qiu³, Yunlong Xiang^{1,2}, Feng Kong^{1,2}, Fangnong Lai^{1,2}, Mrinmoy Pal[®], Peizhe Wang ®⁷, Jia Ming⁷, Bingjie Zhang^{1,2}, Qiujun Wang ®^{1,2}, Jingyi Wu^{1,2}, Weikun Xia^{1,2}, Weimin Shen^{2,5}, Jie Na ®⁷, Maria-Elena Torres-Padilla ®⁶, Jing Li ®^{3,4} & Wei Xie ®^{1,2}

Dynamic epigenomic reprogramming occurs during mammalian oocyte maturation and early development. However, the underlying transcription circuitry remains poorly characterized. By mapping cis-regulatory elements using H3K27ac, we identified putative enhancers in mouse oocytes and early embryos distinct from those in adult tissues, enabling global transitions of regulatory landscapes around fertilization and implantation. Gene deserts harbour prevalent putative enhancers in fully grown oocytes linked to oocyte-specific genes and repeat activation. Embryo-specific enhancers are primed before zygotic genome activation and are restricted by oocyte-inherited H3K27me3. Putative enhancers in oocytes often manifest H3K4me3, bidirectional transcription, Pol II binding and can drive transcription in STARR-seg and a reporter assay. Finally, motif analysis of these elements identified crucial regulators of oogenesis, TCF3 and TCF12, the deficiency of which impairs activation of key oocyte genes and folliculogenesis. These data reveal distinctive regulatory landscapes and their interacting transcription factors that underpin the development of mammalian oocytes and early embryos.

Enhancers are *cis*-distal regulatory sequences that can activate promoters over great distances^{1,2}. They are typically bound by transcription factors (TFs)³ and are marked by distinct epigenetic signatures⁴⁻⁶. Active enhancers frequently bear histone acetylation, such as H3K27ac⁷, which helps activate enhancers by attenuating nucleosome stability, increasing chromatin accessibility and promoting enhancer–promoter communication^{4,8}. Many active enhancers also exhibit enhancer RNAs (eRNAs), which are often bidirectionally transcribed and could be detected by nascent RNA-seq and cap analysis of gene expression sequencing (CAGE)^{9,10}.

 $The \ oocyte-to-embryo \ transition \ (OET) \ features \ a \ transcriptionally \ quiescent \ period \ starting \ from \ the \ end \ of \ oocyte \ growth \ to \ zygotic$

genome activation (ZGA) accompanied by dramatic epigenetic reprogramming ¹¹⁻¹³. Of note, oocytes and early embryos are often subjected to unique or 'non-canonical' transcription and epigenetic regulation. In mice, H3K4me3 exists as widespread non-canonical, broad domains in oocytes and early embryos before ZGA¹⁴⁻¹⁶. H3K27me3 occurs pervasively in the oocyte genome, occupying most regions without transcription¹⁷. Such non-canonical H3K27me3 persists after fertilization until the blastocyst stage and plays a critical role in regulating DNA methylation-independent imprinting and X chromosome inactivation¹⁸⁻²⁰. Moreover, the higher-order chromatin organization in oocytes and early embryos is also distinct from that in somatic cells. For example, the repressive lamina-associated domains (LADs), which usually

A full list of affiliations appears at the end of the paper. Me-mail: ljwth@njmu.edu.cn; xiewei121@tsinghua.edu.cn

occupy gene deserts²¹, are absent in fully grown oocytes (FGOs) and are established de novo after fertilization²². However, how this epigenetic reprogramming facilitates transcriptional changes during OET remains elusive in mammals. Cis-regulatory elements (CREs), such as enhancers, are central in the interplay between chromatin and transcription but are still poorly defined in mammalian oocytes and early embryos. How CREs interact with TFs to elicit transcription in this period remains unclear. Notably, early reports suggested that mouse oocytes and zygotes may even lack enhancer activity based on enhancer reporter assays^{23,24}. Here, we presented a complete putative enhancer map from mouse oogenesis to post-implantation development. These data revealed distinctive epigenetic signatures of enhancers in oocytes and early embryos. We further showed that putative enhancers are often bidirectionally transcribed and can drive reporter activities in oocytes. Notably, these *cis*-regulome maps revealed their potential interacting TFs, leading to the identification of key TFs TCF3 and TCF12 that direct oocyte development.

Results

Dynamic CRE activities in mouse oocytes and early embryos

To identify possible CREs in mouse oocytes and early embryos, we performed H3K27ac STAR chromatin immunoprecipitation (IP) sequencing (ChIP-seq)¹⁶ in growing oocytes (GOs) at postnatal day 7 (GO-P7) and day 10 (GO-P10) stages, FGOs at postnatal week 8, metaphase II (MII) oocytes and mouse early embryos at the one-cell, early two-cell, late two-cell and eight-cell stages and inner cell mass (ICM) from blastocysts (Fig. 1a and Methods). Consistent with the immunostaining results (Extended Data Fig. 1a) and the previous studies^{25,26}, STAR ChIP-seq did not detect H3K27ac enrichment in MII oocytes, which was thus excluded from subsequent analysis (Fig. 1a and Extended Data Fig. 1a,b). H3K27ac ChIP-seq data were well reproduced in replicates (Extended Data Fig. 1b,c). As validations, the promoter H3K27ac levels correlated with stage-specific gene expression (Fig. 1b, left and Extended Data Fig. 2a). Large fractions of H3K27ac peaks (75.4-86.3%) were in distal regions (2.5 kb away from the transcription start sites; TSSs) (Fig. 1a, left), indicating putative enhancers. Distal H3K27ac correlated with chromatin accessibility 19,27 (Extended Data Fig. 2b) and resided near active genes (non-transcribing stages excluded) (Extended Data Fig. 2c). We refer to these distal regions as putative enhancers, hereafter.

Two enhancer transitions around fertilization and implantation

Combined with H3K27ac data in post-implantation embryos that we previously generated²⁸, we mapped a complete landscape of H3K27ac from oocytes to post-implantation embryos (Fig. 1a). The hierarchical clustering showed two clear transitions of H3K27ac upon OET (as reported²⁹) and implantation (Fig. 1c), indicating dramatic epigenetic reprogramming during these periods. This was largely paralleled by the dynamics of the transcriptome during the same period (Fig. 1d and Extended Data Fig. 3). Of note, embryos at the 1-cell and 2-cell stages were clustered with oocytes in transcriptome analyses, presumably due to their inherited maternal RNAs (Fig. 1d). Distal H3K27ac levels seemed to increase from GO-P7 to GO-P10 and elevated further in FGOs at oocyte-specific putative enhancers (Fig. 1b, right), consistent with the immunofluorescence results (Extended Data Fig. 1a). We then identified 63,657, 42,409 and 37,590 distal H3K27ac sites as putative enhancers in mouse oocytes, pre- and post-implantation embryos, respectively. Notably, comparison with those from a panel of tissues (n = 94) from ENCODE³⁰ showed oocytes possessed a large fraction of unique enhancers (n = 31,838,47.7%), in contrast to pre-implantation embryos (n = 6,581, 9.7%) and post-implantation embryos (n = 7,855, 11.9%) (Fig. 1b, right, discussed below). Similar to global H3K27ac, distal H3K27ac-defined putative enhancers also displayed two waves of transitions during fertilization and implantation (Fig. 1b, right).

Such transitions were also observed at repeats. H3K27ac peaks were enriched for MaLR and ERVK in oocytes (Extended Data Fig. 4), consistent with previous findings³¹. H3K27ac peaks in pre-implantation embryos were enriched for ERV and SINE elements, including B1/B2/B4, agreeing with them being preferentially accessible at these stages²⁷. Post-implantation embryos were relatively enriched for mammalian-wide interspersed repeat (MIR) and LINE2 (L2) (Extended Data Fig. 4). Taken together, these data reveal two global regulome transitions centred around fertilization and implantation.

Prevalent H3K27ac in gene deserts in FGOs

Given that oocytes possess many unique enhancers, we sought to characterize them in greater details. During oocyte growth, a transcription switch occurred between GO-P7 and GO-P10, correlated with promoter H3K27ac changes (Extended Data Fig. 5a). For example, Hexb, Sohlh1 and Sohlh2, three genes expressed in GO-P7 but not in GO-P10, showed strong promoter H3K27ac only in GO-P7 (Extended Data Fig. 5b). Oosp1, Oosp2 and Oosp3 genes32 were highly induced starting from P10, consistent with increased H3K27ac at their promoters (Extended Data Fig. 5b). Distal H3K27ac was also highly dynamic during oocyte growth (Fig. 2a). Compared to GOs and adult somatic tissues, FGOs showed the most stage-specific putative enhancers (44.3%, n = 18,200) (Fig. 2b). Further analysis showed that FGOs exhibited increased H3K27ac (Fig. 2c,d), gene expression (Extended Data Fig. 5c, left) and active repeats (Extended Data Fig. 5c, right, and Extended Data Fig. 5d) in gene-poor regions or gene deserts (Methods). For example, the Oosp gene cluster is present in gene deserts (Extended Data Fig. 5b, right). In sum, these data revealed prevalent H3K27ac and potential regulatory activities in gene deserts in FGOs linked to oocyte-specific genes and repeats.

Allelic reprogramming of H3K27ac after fertilization

We then examined H3K27ac in early embryos, by separating allelic signals using single-nucleotide polymorphisms (SNPs) present between the two parental strains (Fig. 2e and Methods). Upon meiotic resumption, H3K27ac is quickly erased in MII oocytes (Extended Data Fig. 1a) due to the recruitment of histone deacetylases to metaphase chromatin^{25,26,29}. After fertilization, H3K27ac reappears at the pronuclear stage 3 to pronuclear stage 4 (ref. 33). A comparison of sperm and zygote paternal H3K27ac revealed distinct patterns (Fig. 2e,f), suggesting rapid paternal reprogramming upon fertilization, similar to that for H3K4me3 and H3K27me3 (refs. 16,17). Notably, the maternal allele of the PN5 zygote showed H3K27ac enrichment that partially resembled that of FGOs (Fig. 2e,f), suggesting that regulatory elements may be bound by the inherited maternal factors in the one-cell embryos. However, H3K27ac in gene-poor regions showed an evident decrease after fertilization (Fig. 2e,g, 'gene-poor'). H3K27ac peaks lost in the one-cell embryos enriched for similar TF motifs as those that retained H3K27ac compared with FGOs (Extended Data Fig. 6a, discussed later), suggesting that the absence of these peaks is not due to the loss of maternal TFs, but is likely related to the chromatin reorganization. The exact mechanisms underlying such depletion of H3K27ac in gene deserts remained to be determined. Notably, LADs are absent in FGOs and are de novo established after fertilization in mice²². Consistently, the strengths of the genome-lamina interaction and H3K27ac were anti-correlated in early embryos and mouse embryonic stem (mES) cells, except on the maternal allele of the one-cell embryos (R = 0.20) (Extended Data Fig. 6b), which was shown to feature fragmented LADs²². Given the enrichment of H3K27ac in gene deserts appeared as early as GO-P10 (Fig. 2b), we thus asked whether LADs were already absent at GO-P10 stage using DNA adenine methyltransferase identification (DamID)²². Indeed, Dam-lamin B1 profiles suggested the absence of LADs at this stage (Extended Data Fig. 6c). We could not map LADs in an even earlier stage such as GO-P7 due to the difficulty of performing robust microinjection given their smaller sizes. In sum, these

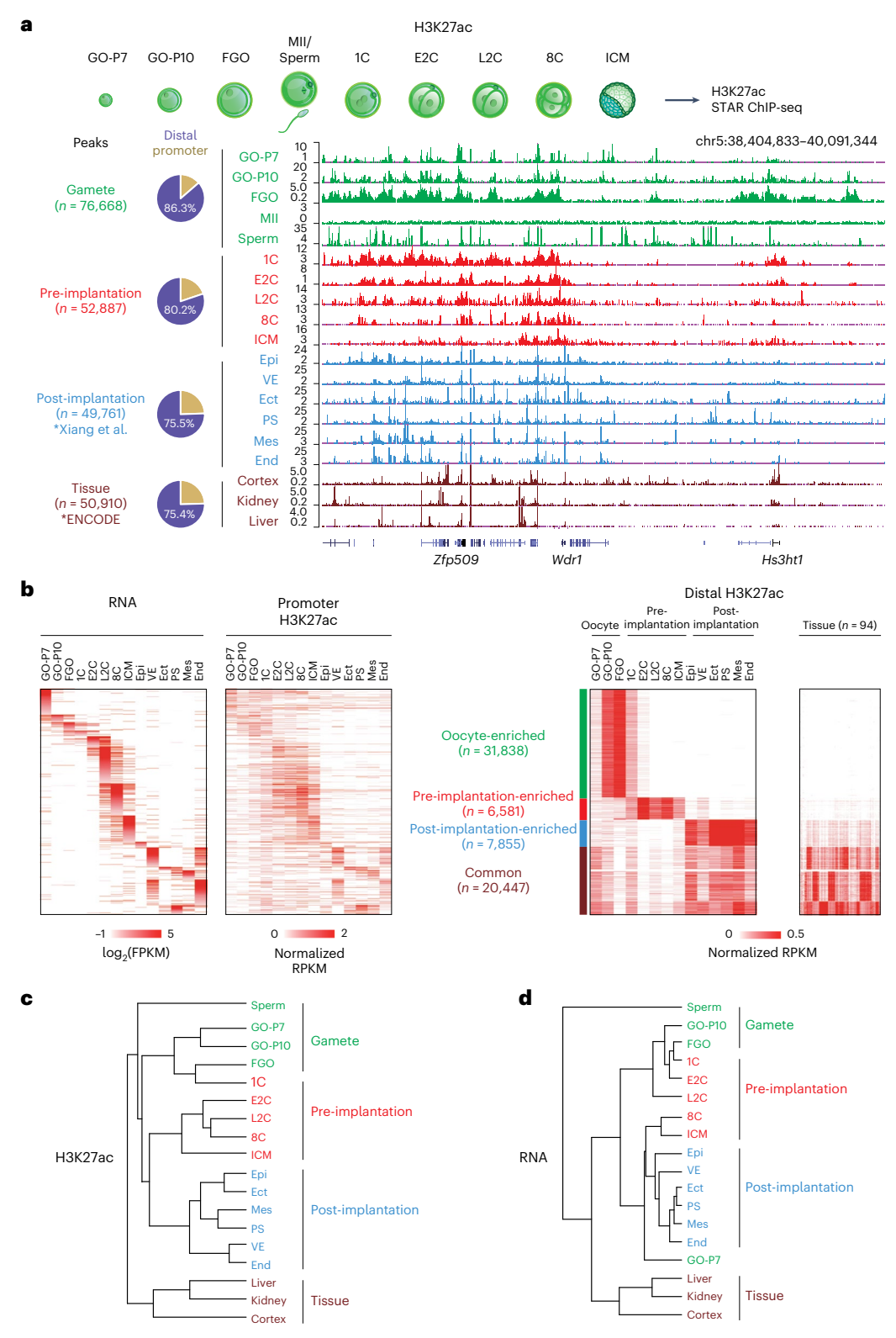


Fig. 1| **H3K27ac landscape in mouse gametes, early embryos and tissues. a**, Schematic showing the overview of H3K27ac STAR ChIP-seq in mouse gametes and early embryos. The UCSC browser view shows H3K27ac signals in gametes (GO-P7, GO-P10, FGO, MII oocyte and sperm), pre-implantation embryos (one-cell PN5, early two-cell, late two-cell, eight-cell and ICM), post-implantation embryos (Epi, VE, Ect, PS, Mes and End) and tissues (cortex, kidney and liver). Pie charts show H3K27ac peak distribution at the promoter and distal regions. Epi, epiblast; VE, visceral endoderm; Ect, ectoderm; PS, primitive streak; Mes, mesoderm; End, endoderm. **b**, Heatmaps showing the stage-specific

gene expression and H3K27ac signals for the corresponding promoters (left). Heatmaps showing the oocyte- (GO-P7, GO-P10 and FGO), pre-implantation- (one-cell, early two-cell, late two-cell, eight-cell and ICM), post-implantation- (Epi, VE, Ect, PS, Mes and End) enriched and common putative active enhancers marked by distal H3K27ac (right). H3K27ac signals of 94 mouse tissues are also mapped. ${\bf c}$, Hierarchical clustering of global H3K27ac in 2-kb bins. ${\bf d}$, Hierarchical clustering of gene expression across all stages. Source numerical data are available in source data.

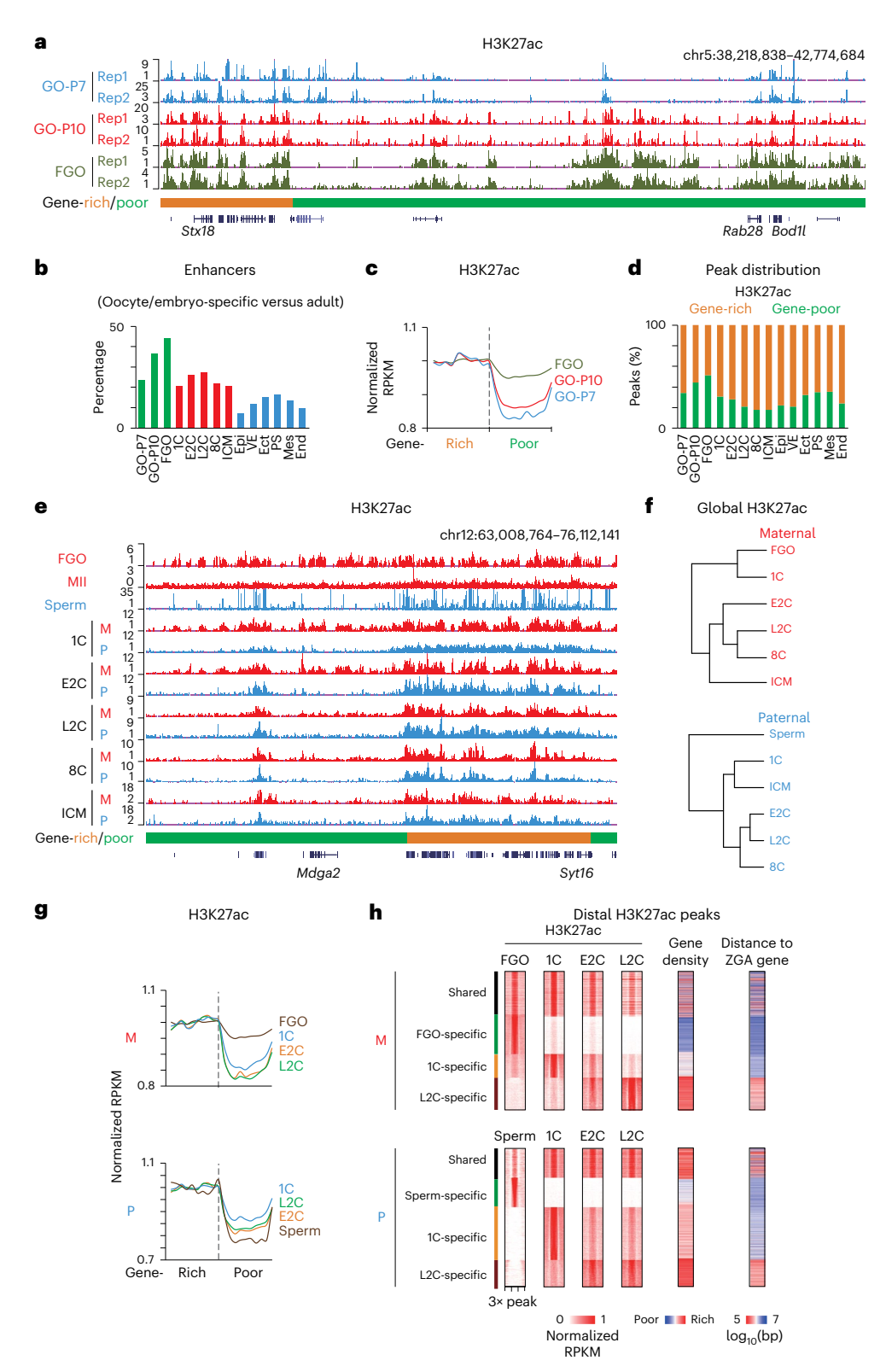


Fig. 2 | **Reprogramming of H3K27ac in mouse gametes and early embryos. a**, The UCSC browser view showing H3K27ac signals in GO-P7, GO-P10 and FGOs with two replicates. Gene-rich (orange) and gene-poor (green) regions are also shown. **b**, Bar chart showing the percentages of the unique enhancers at each stage compared with adult tissues. **c**, Line chart showing normalized H3K27ac signals of GO-P7, GO-P10 and FGO at gene-rich regions and the nearby gene-poor regions. **d**, Bar chart showing distributions of H3K27ac peaks in gene-rich (orange) and gene-poor (green) regions at each stage. **e**, The UCSC browser view showing allelic H3K27ac signals in FGO, MII oocytes, sperm, PN5 zygote, early two-cell, late two-cell, eight-cell and ICM. M, maternal (red). P, paternal (blue).

Gene-rich and gene-poor regions are also shown. **f**, Hierarchical clustering of FGOs and early embryos on allelic H3K27ac enrichment. For FGO and sperm H3K27ac data, only regions covered by SNPs were included for analysis. **g**, Line charts showing normalized H3K27ac signals in gene-rich and gene-poor regions in gametes (FGO and sperm) and early embryos (one-cell, early two-cell and late two-cell). M, maternal; P, paternal. **h**, Heatmaps showing distal H3K27ac signals, gene density and distance to nearby ZGA genes at shared, FGO/sperm-specific, one-cell-specific and late two-cell-specific allelic peaks. Source numerical data are available in source data.

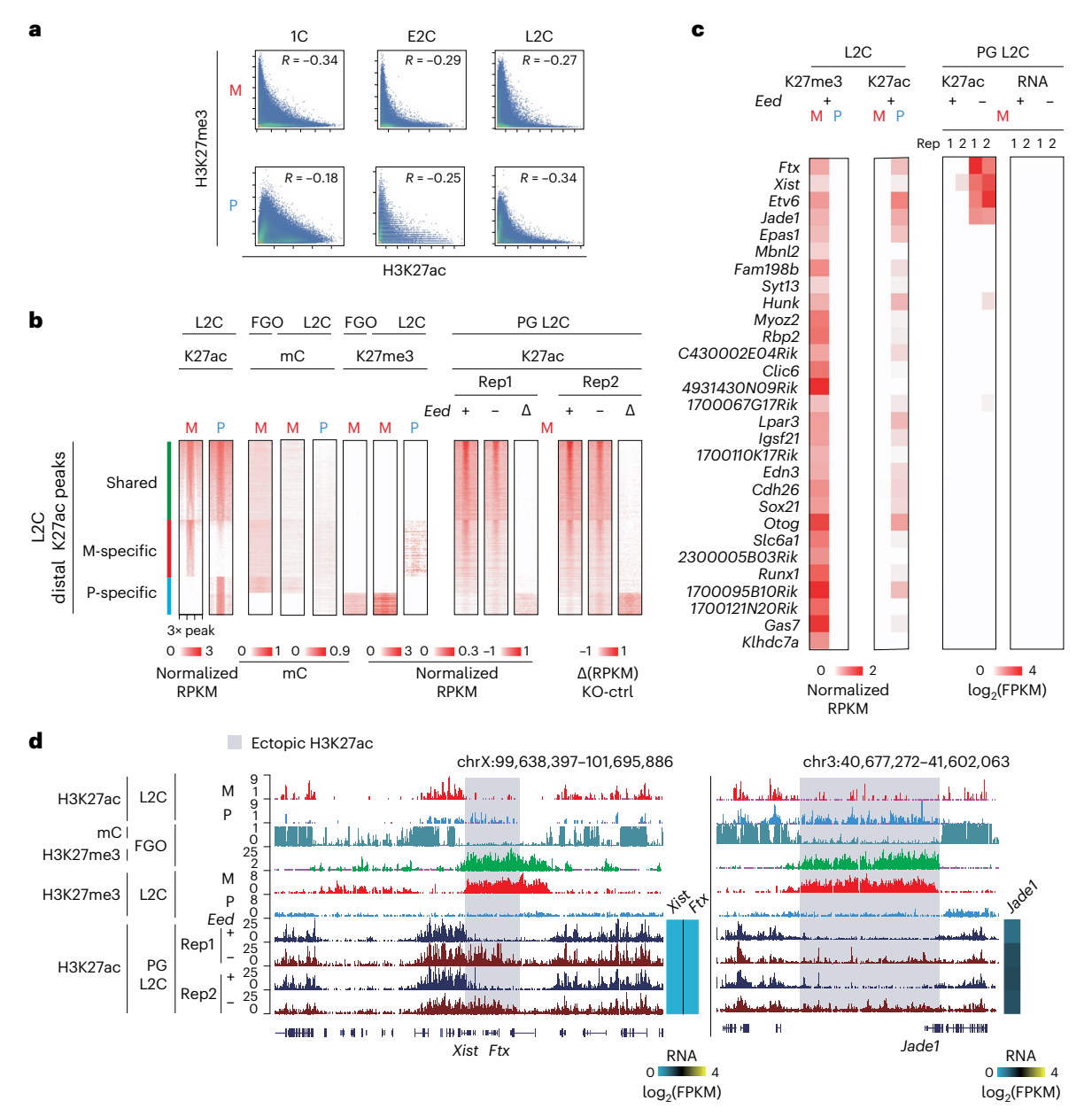


Fig. 3 | **Reprogramming of H3K27ac and H3K27me3 during ZGA. a**, Scatter-plots comparing allelic H3K27ac and H3K27me3 in the one-cell, early two-cell and late two-cell embryos. M, maternal. P, paternal. Pearson correlations of each stage are also shown. **b**, Heatmaps showing H3K27ac, DNA methylation (mC) and H3K27me3 signals at late two-cell H3K27ac maternal-specific (red) and paternal-specific (blue) peaks in WT (left) and parthenogenetic (PG) *Eed* control and KO late two-cell embryos (right). **c**, Heatmaps showing H3K27me3, H3K27ac signals

and RNA at H3K27me3-imprinting genes in WT, parthenogenetic *Eed* control and KO late two-cell embryos. M, maternal. P, paternal. d, The UCSC browser view showing H3K27me3, H3K27ac and mC signals of WT late two-cell and FGO, parthenogenetic control and *Eed* knockout late two-cell embryos at *Xist*, *Ftx* and *Jade1*. Heatmaps show RNA expression of related genes. Ectopic H3K27ac is shaded.

results suggest that after fertilization, the paternal H3K27ac undergoes reprogramming and the maternal H3K27ac adopts an FGO-like pattern, while losing enrichment in gene-poor regions.

At the late two-cell stage, H3K27ac distal peaks preferentially resided in gene-rich regions and were proximal to major ZGA genes (Fig. 2d,h). Notably, early two-cell embryos manifested an intermediate H3K27ac state between those of the one-cell and late two-cell embryos, as they already bore H3K27ac in sites destined to be activated in late two-cell embryos (Fig. 2h), suggesting chromatin priming before major ZGA. This finding echoes the 'pre-configuration' of RNA polymerase II (Pol II) to major ZGA genes at the early two-cell stage³⁴. Therefore, these data indicate that the activities of H3K27ac-marked regulatory elements also undergo pre-configuration before ZGA.

Maternal H3K27me3 represses putative embryonic enhancers

H3K27ac undergoes erasure in MII oocytes and re-establishment after fertilization (Fig. 2e and Extended Data Fig. 1a). Yet, how H3K27ac is re-established remains elusive. Maternally deposited H3K27me3 represses enhancers during ZGA in $Drosophila^{35}$. Oocyte-derived H3K27me3 is also inherited in mouse early embryos and regulates gene imprinting Notably, H3K27me3 is mutually exclusive with H3K27ac in the one-cell and two-cell embryos (Fig. 3a). Therefore, we asked whether the activities of embryonic enhancers around ZGA are affected by oocyte-inherited H3K27me3 in mouse embryos. We deleted Eed in oocytes using Gdf9-Cre, erasing H3K27me3 globally 36 . Due to limited SNPs between the parental strains which prevented allele distinction in embryos (Methods), we obtained parthenogenetically activated

(PG) late two-cell embryos from $Eed^{-/-}$ oocytes and profiled H3K27ac. We first identified regions that showed paternal-specific H3K27ac in wild-type (WT) embryos and further classified them into those marked by H3K27me3 or DNA methylation on the maternal allele. Indeed, we observed ectopic H3K27ac in maternal H3K27me3-marked regions in $Eed^{-/-}$ PG embryos (Fig. 3b, right, ' \triangle '). These regions included, but were not limited to, a subset of the H3K27me3-controlled imprinted regions such as Xist, Etv6 and Jade1 (Fig. 3c,d). Nevertheless, these imprinted genes remained silenced based on the RNA-seq analyses (Fig. 3c, 'RNA'). We speculate that additional regulators, such as key TFs, are necessary for the ultimate activation of these genes. Thus, oocyte-inherited H3K27me3 represses putative embryonic enhancers in mouse embryos.

H3K4me3 marks enhancers in oocytes and pre-implantation embryos

Previously, we found that somatic enhancers were aberrantly activated and acquired H3K4me3 in dnmt1-deficient zebrafish early embryos that lost DNA methylation³⁷. As mammalian oocytes and embryos are naturally hypomethylated^{38,39}, we asked whether their putative enhancers may be also susceptible to acquiring H3K4me3. In line with previous work²⁹, distal H3K27ac sites were preferentially marked by H3K4me3 in oocytes and pre-implantation embryos, but were less so in post-implantation embryos, which became DNA hypermethylated (Fig. 4a). Consistent with the antagonism between H3K4me3 and DNA methylation in FGOs⁴⁰, putative enhancers with high levels of DNA methylation showed low levels of H3K4me3 in WT FGOs but acquired H3K4me3 in *Dnmt3a/b* mutant FGOs (Fig. 4b and Extended Data Fig. 7a). This result echoed a similar finding for enhancers in *Dnmt3a/b* double knockout mES cells (Extended Data Fig. 7b). One exception is GO-P7, where the entire genome is DNA hypomethylated ⁴¹ but the enhancers did not show strong H3K4me3 enrichment (Fig. 4a), suggesting that additional mechanisms may exist to prevent H3K4me3 deposition. H3K4me3 is closely associated with RNA Pol II, including that at enhancers⁴². Consistently, enhancers with the H3K4me3-H3K27ac dual mark were more likely to be bound by Pol II and showed shorter distances to nearby active genes compared with H3K27ac-only enhancers (Extended Data Fig. 7c,d). Finally, in oocytes (except GO-P7) and pre-implantation embryos, but not post-implantation embryos, H3K4me3/H3K27ac dual-marked and H3K27ac-only distal regions showed comparable enrichment for distal CREs identified by ENCODE⁴³ (Extended Data Fig. 7e). Taken together, H3K4me3 also marks a portion of putative active enhancers in oocytes and pre-implantation embryos, a feature that is closely linked to global DNA hypomethylation.

Oocyte enhancers are transcribed and drive reporter expression

We then sought to functionally validate putative enhancers in oocytes. Given eRNAs were shown to be a reliable marker for active enhancers^{44,45}, we took advantage of a CAGE dataset in mouse GO-P14 oocytes⁴⁶ to assess whether putative enhancers were transcribed (Fig. 4c). CAGE allows the mapping of the transcription initiation sites of unidirectional transcribed RNAs at TSSs and bidirectionally transcribed RNAs preferentially at enhancers¹⁰. We identified 7,157 unidirectionally and 2,786 bidirectionally transcribed sites using CAGEr⁴⁷ and CAGEfightR⁴⁸ (Fig. 4c and Methods). To strictly exclude promoters, we used an expanded promoter annotation that included defined TSSs of de novo assembled oocyte transcripts using deep-depth RNA-seq data31 and pooled promoters from a panel of somatic cells (191,499 H3K4me3 sites from 26 tissues from ENCODE⁴⁹). These data confirmed that unidirectionally transcribed sites predominantly (99.5%) enriched for promoters (overlapping with expanded oocyte TSSs, somatic H3K4me3 sites or both). By contrast, only 60.6% of bidirectionally transcribed sites overlapped with annotated promoters. We considered the rest 39.4% as 'CAGE-enhancers' (n = 1,097; Methods). The small number of CAGE-enhancers was likely an underestimation of enhancers in oocytes considering the limited sensitivity of low-input CAGE. Reassuringly, 91.4% of CAGE-enhancers overlapped with H3K27ac (compared with 16.2% of random sites) (Extended Data Fig. 7f). Overall, 90.8% were also occupied by H3K4me3 (compared with 20.5% of random sites) and 83.4% were marked by both marks (compared with 7.3% of random sites). Consistent with the essential roles of histone acetylation in transcription⁵⁰, removing histone acetylation in NSN-FGO by Plumbagin, an inhibitor for histone acetyltransferases (HATs)⁵¹, blocked transcription as measured by EU staining (Extended Data Fig. 8a,b). On the other hand, the role of H3K4me3 at enhancers remains elusive. H3K4me3 at enhancers is reported to cause enhancer overactivation⁵². Yet, a mutation in Mll2, which encodes an H3K4me3 methyltransferase in oocytes, caused a substantial reduction of non-promoter H3K4me3, which had little correlation with transcription defects⁴⁰. However, a detailed analysis showed that 83.3% of CAGE-enhancers 46 and 52.5% of H3K4me3-marked distal H3K27ac sites still retained H3K4me3 upon the ablation of Mll2 (Extended Data Fig. 8c,d). Therefore, it remains to be determined whether H3K4me3 is functional at these putative enhancers. Taken together, these data show that putative enhancers in oocytes are often marked by H3K4me3, H3K27ac and bidirectional transcription.

To further validate the putative enhancers in oocytes, we employed self-transcribing active regulatory region sequencing (STARR-seq)⁵³. We optimized the STARR-seq protocol for low-input samples with an improved RNA recovery method adapted from Smart-seq2 (ref. 54; Methods and Extended Data Fig. 9a). As the limited oocytes were insufficient to support the assessment of all enhancers, we constructed the STARR-seg plasmid library by manually cloning 70 enhancer candidates with strong bidirectional CAGE signals and distal H3K27ac peaks (84% also carried H3K4me3, n = 59) (Fig. 4d, 'CAGE +') (Methods) and 16 negative regions (regions with neither CAGE signals nor H3K27ac in oocytes, including two putative embryo-specific enhancers near Nanog and Fgf3) (Fig. 4d,e). We also tested whether H3K27ac alone, without CAGE signals, can mark active enhancers by cloning two such putative enhancer sites near Nobox and Bmp15 (Fig. 4d, 'CAGE-'). The STARR-seq plasmid library was injected into the nuclei of FGOs and RNAs were extracted for sequencing. Our results showed that 64% (45 of 70, with 37 out of 45 (82%) carrying H3K4me3) of putative enhancers showed bidirectional activities, compared with none (0 of 16) from the negative controls ($P = 1 \times 10^{-6}$; Fig. 4e and Extended Data Fig. 9b). For example, on chromosome 16, all three candidate sites, but not the negative control. showed strong STARR-seq RNA signals (Extended Data Fig. 9c). While most of these elements enhanced reporter activities in both orientations, some did exhibit stronger activation abilities for one orientation than the other (Fig. 4e), echoing the observation that enhancers are largely but not completely orientation-independent^{55,56}. Moreover, the putative enhancers near *Nobox* and *Bmp15* with no CAGE signals only showed weak STARR-seq signals, often for only one orientation (Fig. 4f, 'CAGE -'), raising the possibility that CAGE together with H3K27ac may be a better mark for active enhancers than H3K27ac alone. To further validate these enhancers, we cloned seven candidate enhancers that showed positive STARR-seq signals, four negative controls (including embryo-specific enhancer candidates near Nanog and Fgf3) and the two 'CAGE -' candidate enhancers near Nobox and Bmp15 into the GFP (mNeonGreen) reporter (Fig. 4g, Extended Data Fig. 9d,e and Methods). A Zp3 promoter-driven mCherry construct was co-injected as a control to normalize GFP signals. Our data showed that 100% (7 out of 7) of positive candidates, but neither the four negative controls nor the two 'CAGE -' candidates near Nobox and Bmp15, showed enhanced GFP expression compared with the empty vector (Fig. 4g and Extended Data Fig. 9d,e). Notably, these positive enhancers also preferentially showed Pol II binding in FGOs³⁴, compared with 'CAGE -' enhancers and negative controls (Fig. 4g and Extended Data Fig. 9d; 'Pol II'). Genome-wide analyses also showed that distal H3K27ac sites associated with Pol II tended to have strong H3K4me3 and CAGE signals and were closer to

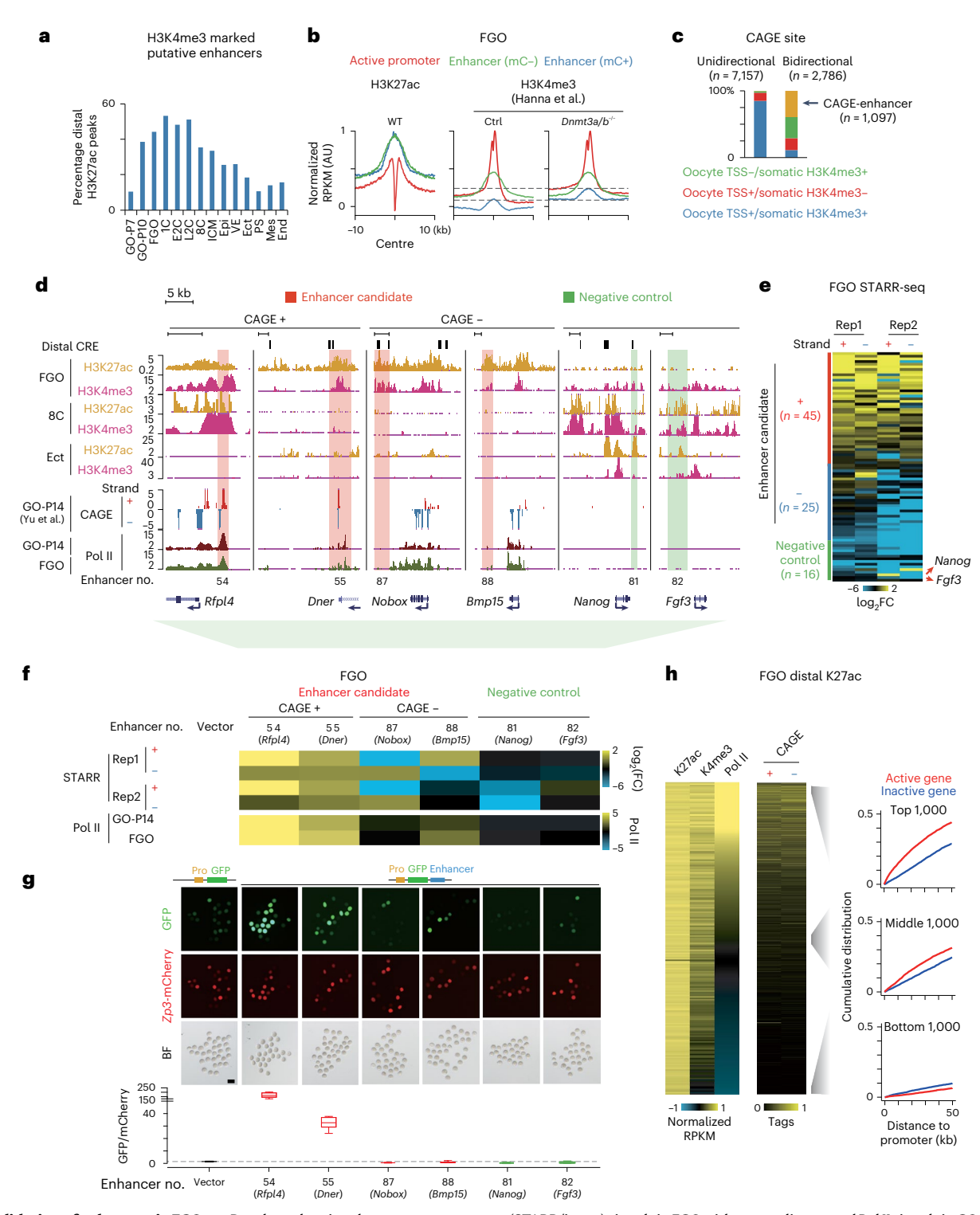


Fig. 4 | **Validation of enhancers in FGOs. a**, Bar chart showing the percentages of H3K4me3-marked putative enhancers (marked by H3K27ac) at each stage from oocytes to post-implantation embryos. **b**, Line charts showing H3K27ac and H3K4me3 signals at putative enhancers with low (green) or high (blue) DNA methylation and active promoters (red) in WT (left), control (middle) and Dnmt3a/Dnmt3b KO (right)⁴⁰ FGOs. The dashed lines indicate the peaks of H3K4me3 signals at putative enhancer regions. **c**, Bar chart showing the overlap between uni- or bidirectional CAGE sites and oocyte TSSs or somatic H3K4me3 sites. **d**, The UCSC browser views showing H3K27ac and H3K4me3 enrichment and CAGE signals near oocyte candidate enhancers and negative controls. **e**, Heatmaps showing FGO STARR-seq signals (STARR/input) for enhancer candidates (n = 70) and negative controls (n = 16, including putative embryospecific enhancers near Nanog and Fgf3). **f**, Heatmaps showing STARR-seq

(STARR/input) signals in FGO with two replicates and Pol II signals in GO-P14 and FGO at enhancer candidates (orange shade in **d**) and negative control (green shade in **d**) regions. **g**, Top, fluorescence and bright fields of mouse FGOs in the enhancer reporter assay (Pro, minimal promoter). Scale bar, $100 \, \mu m$. Boxplot showing the ratio of GFP to mCherry intensity in the enhancer reporter assay (bottom). The numbers of oocytes used in each group: 17, 18, 15, 13, 10, 11 and 6. The median is indicated by the centre line. The bottom, top edges and whiskers represent the $10 \, \mu m$ 10th and $1.5 \, \mu m$ 20th percentiles and $1.5 \, \mu m$ 20th respectively. The dashed line indicates the ratio in the empty vector group. **h**, Heatmaps showing H3K27ac, H3K4me3 and CAGE signals at all distal H3K27ac peaks in FGOs (ranked by Pol II signals) (left). Line charts showing the cumulative distribution of the distances between promoters of active and inactive genes (top 5,000) and nearest distal H3K27ac sites (top, middle and bottom 1,000 peaks) (right).

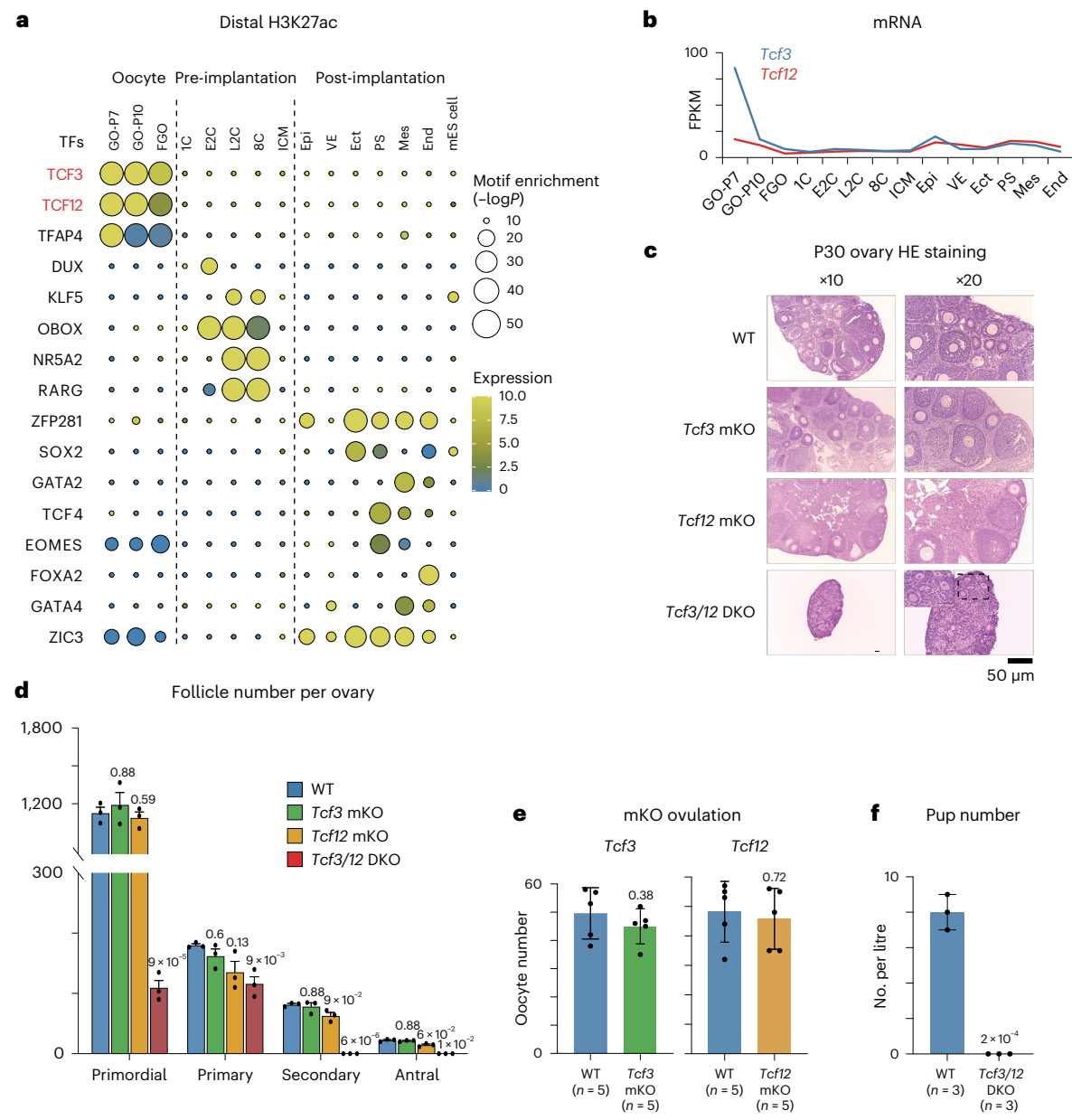


Fig. 5 | Identification of candidate TF regulators from putative enhancer maps during oogenesis and pre-implantation embryos. a, Transcription factor motifs identified from distal H3K27ac peaks at each stage in mouse oocytes (GO-P7, GO-P10 and FGO), embryos (one-cell, early two-cell, late two-cell, eight-cell, ICM from blastocyst, Epi, VE, Ect, PS, Mes and End and ES cells. Each circle represents a distinct TF motif, with the colour indicating the RNA expression level and the size indicating the enrichment of the motif ($-\log_{10} P$ value, hypergeometric test with Bonferroni correction, one-sided, from HOMER⁵⁷; Methods). **b**, Line chart showing RNA levels of Tcf3 and Tcf12 in oocytes and early embryos. **c**, Haematoxylin and eosin (H&E) staining of ovary sections

from WT, Tcf3 mKO, Tcf12 mKO and Tcf3/12 DKO mice at postnatal day 30. Scale bar, 50 µm. **d**, Bar chart showing the follicle numbers of WT (blue), Tcf3 mKO (green), Tcf12 mKO (yellow) and Tcf3/12 DKO (red) P30 ovaries (n=3 biological replicates). P value (t-test, two-sided) is also shown. The error bars represent the s.e.m. **e**, Bar charts showing ovulation rates in WT and Tcf3 (left) or Tcf12 (right) mKO mice (n=5 biological replicates). P value (t-test, two-sided) is also shown. The error bars represent the s.e.m. **f**, Bar chart showing the number of pups per litter in WT and Tcf3/12 DKO mice (n=3 biological replicates, indicated by dots). P value (t-test, two-sided) is also shown. The error bars represent the s.e.m. Source numerical data and unprocessed blots are available in source data.

active genes, indicating they are more likely to be active enhancers (Fig. 4h). These data indicate that active enhancers exist in FGOs as validated by both STARR-seq and the enhancer reporter assay and Pol II and CAGE association provide additional prediction power for active enhancers than H3K27ac alone.

Enhancer maps identify TCF3/12 as key folliculogenesis regulators

Enhancers are bound by cell-type-specific TFs⁷. To further validate these enhancer maps, we performed a motif analysis using HOMER⁵⁷

in distal H3K27ac peaks in oocytes and early embryos to search for potentially interacting TFs (Fig. 5a). Consistent with the previous studies^{27,28}, key factors such as DUX⁵⁸⁻⁶⁰, OBOX^{61,62} and NR5A2 (refs. 63–65) were enriched at the pre-implantation stages. SOX2, GATA2, TCF4 and EOMES were enriched at the post-implantation stages. Of note, no strong TF motif enrichment was present at the one-cell stage and ICM. This was possibly due to the dilution of enrichment by different TF motifs as these stages undergo rapid transitions. Indeed, an analysis with finer gene classification identified similar motifs at the one-cell stage as those in oocytes and two-cell embryos (Extended Data Fig. 6a).

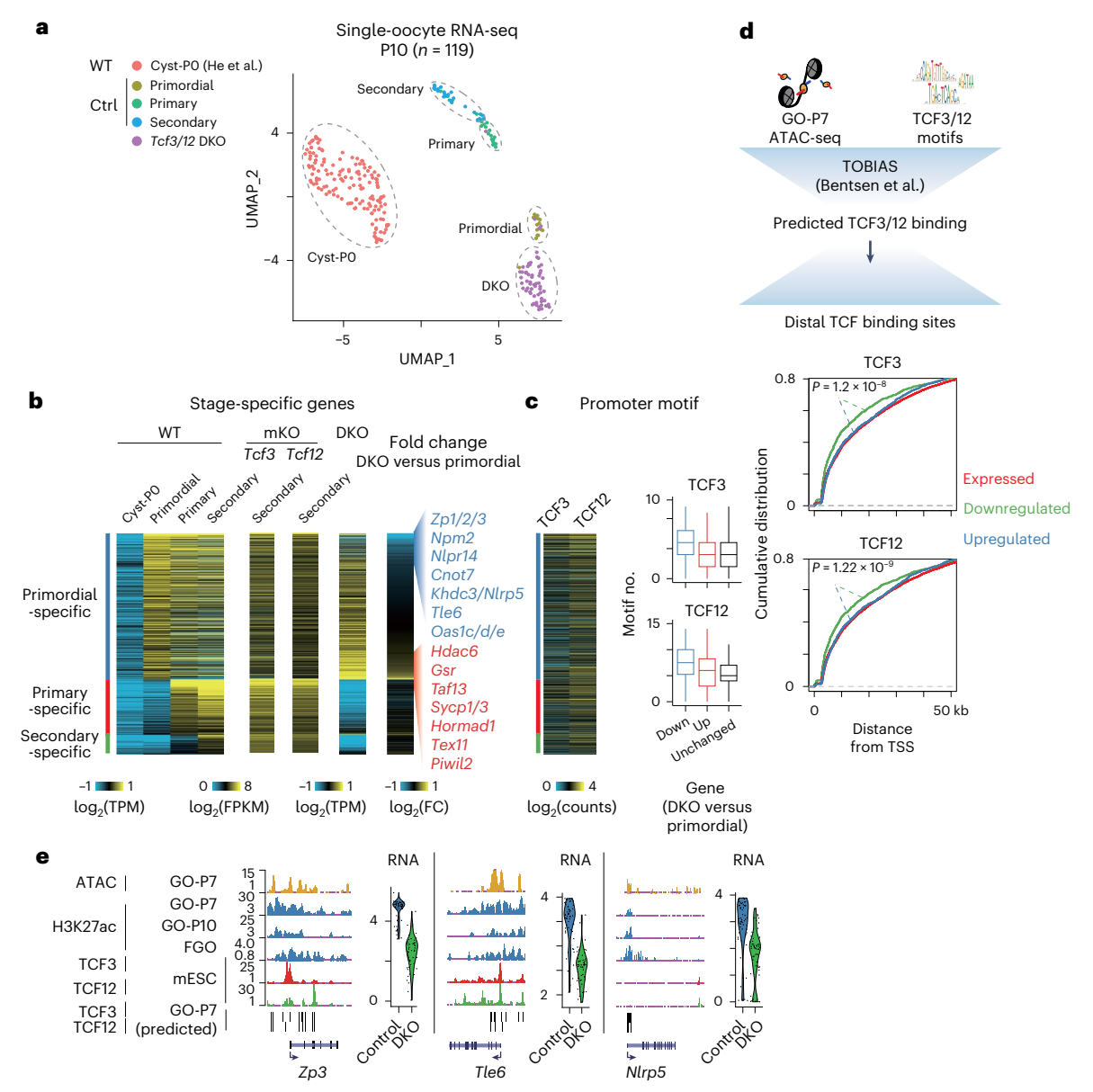


Fig. 6 | **TCF3** and **TCF12** are key folliculogenesis regulators. a, UMAP plot showing the different representations of oocyte clusters from ref. 72, control and Tcf3/Tcf12 DKO GO-P10 ovary by single-oocyte RNA-seq. b, Heatmaps showing the stage-specific gene expression at different stages of WT, Tcf3 mKO, Tcf12 mKO and Tcf3/Tcf12 DKO oocytes. Fold changes of DKO oocytes versus WT oocytes from primordial follicles as well as upregulated and downregulated example genes are also shown. c, Heatmap showing TCF3 and TCF12 promoter motif densities (left). Box plots showing TCF3 and TCF12 promoter motif densities for downregulated (n = 50), upregulated (n = 56) and unchanged genes (n = 923)

(right). The median is indicated by the centre line. The bottom, top edges and whiskers represent the 10th and 90th percentiles and 1.5 × IQR, respectively. **d**, Top, schematic showing TCF3/TCF12 binding prediction by TOBIAS⁷³. Bottom, line charts showing the cumulative distribution of the distance between TSSs of expressed, downregulated and upregulated genes and nearest distal predicted TCF3 (middle) or TCF12 (bottom) binding sites. *P* values, *t*-test, two-sided. **e**, The UCSC browser views and violin plots showing ATAC-seq, H3K27ac, mES cells TCF3/TCF12 signals and RNA expression (normalized) in control and DKO oocytes at representative downregulated genes.

Notably, motifs of TCF12 (HEB), TCF3 (E2A) and TFAP4 seemed to be specific for oocytes (Fig. 5a). These motifs were shared by putative enhancers in both GOs and FGOs, despite their distinct H3K27ac land-scapes, suggesting that the same TFs may actively redistribute in the genome upon oocyte growth. TCF3/TCF12 are basic helix-loop-helix (bHLH) TFs known to play compensatory roles in T cell lineage differentiation and B cell development by forming heterodimers $^{66-68}$. TCF12 also participates in germ layer development in concert with the Polycomb repressive complex 2 (PRC2) 69 . Tcf3 and Tcf12 were expressed in oocytes and early embryos but their expression culminated in GO-P7 (Fig. 5b). FGO enhancers previously identified by STARR-seq also enriched for the TCF3 and TCF12 motifs (Extended Data Fig. 10a,b). Of note, TCF3 could

interact with FIGLA in vitro, a germ cell-specific TF required for ovarian follicle formation and activate zona pellucida genes (Zp1/Zp2/Zp3) in a reporter assay in fibroblast cells^{70,71}. However, whether TCF3/TCF12 regulate oocyte development in vivo remains unknown. Therefore, we generated conditional knockout (KO) mice deficient for either Tcf3 or Tcf12 in oocytes (driven by Gdf9-Cre) (Methods) and confirmed the depletion of Tcf3/Tcf12 in oocytes (Extended Data Fig. 10c and Methods). However, folliculogenesis and ovulation seemed largely normal for Tcf3 maternal knockout (mKO) and Tcf12 mKO oocytes (Fig. 5c-e). Due to the functional compensation and the similar binding motifs of TCF3 and TCF12 (ref. 67), we obtained Tcf3/Tcf12 double KO (DKO) oocytes (Methods) and confirmed the depletion of

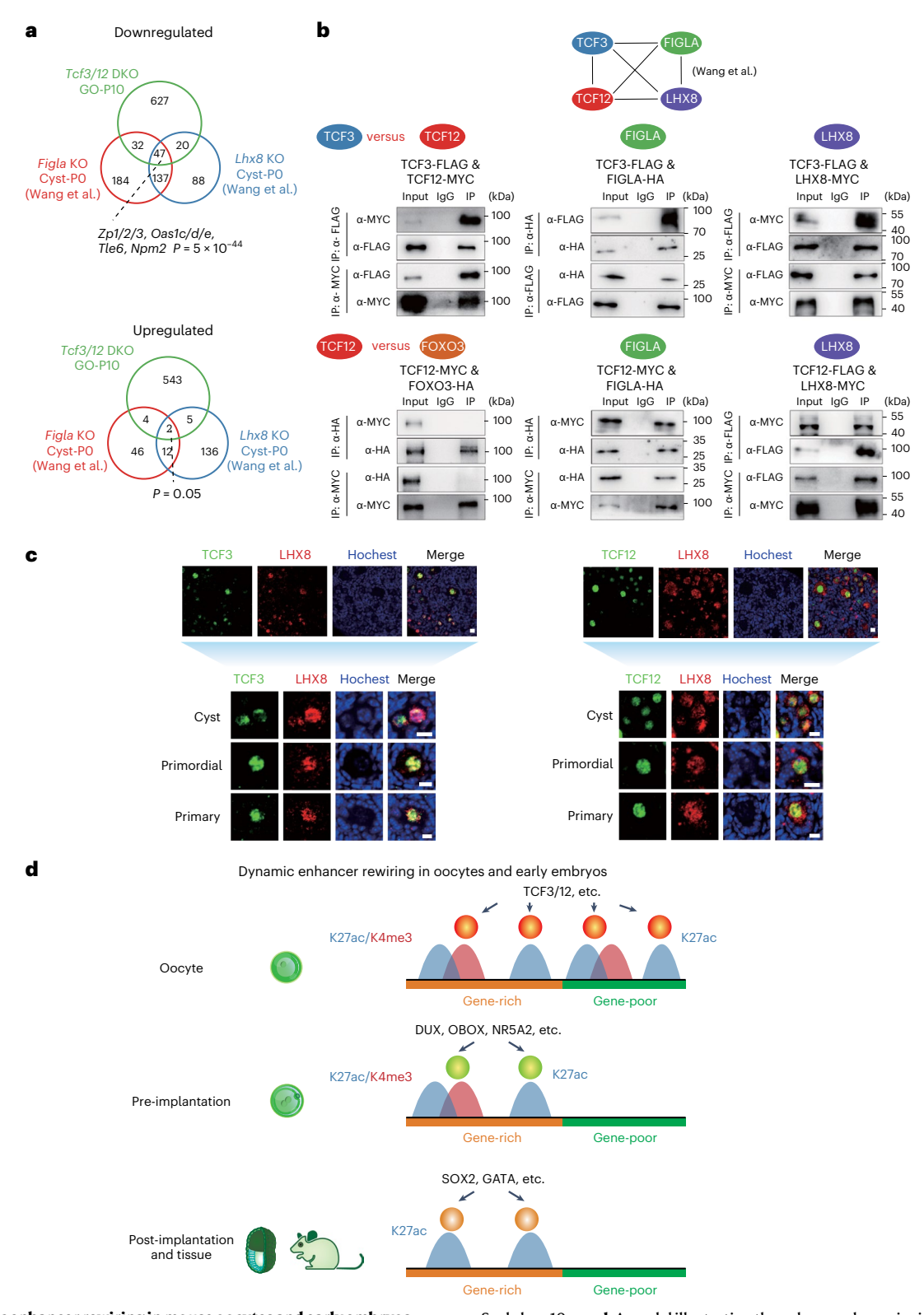


Fig. 7 | Dynamic enhancer rewiring in mouse oocytes and early embryos.

a, Venn diagrams showing the overlap of downregulated (top) and upregulated (host can) groups and a feet (Table 2, Field and Lhard Income and the Charles of th

(bottom) genes among *Tcf3/Tcf12*, *Figla* and *Lhx8* knockout oocytes. *P* values (Fisher's exact test, two-sided) for overlapped genes are also shown. **b**, Schematic of IP results showing pairwise interactions between TCF3, TCF12, FIGLA and LHX8 (top). The interaction between FIGLA and LHX8 is from Wang et al. ⁷⁸. IPs for various TF combinations in HEK293T cells: TCF3 with TCF12, FIGLA, LHX8 and TCF12 with FOXO3 (negative control), FIGLA and LHX8 (bottom). **c**, Immunostaining showing TCF3, TCF12 and LHX8 in oocytes from the cyst, primordial and primary follicles of P2.5 ovary (*n* = 3 biological replicates).

Scale bar, $10 \, \mu m$. **d**, A model illustrating the enhancer dynamics in oocytes and early embryos. In oocytes, putative enhancers reside in both gene-rich and gene-poor regions, potentially interacting with key TFs such as TCF3 and TCF12. A large portion of putative active enhancers bear both H3K4me3 and H3K27ac. After fertilization, putative enhancers are located mainly in gene-rich regions, likely interacting with a new set of TFs, such as DUX, OBOX and NR5A2, in preimplantation embryos. In post-implantation embryos and adult tissues, putative enhancers enrich for motifs for lineage-specific TFs such as SOX2 and GATA and no longer carry H3K4me3 likely due to genome-wide DNA hypermethylation. Source numerical data and unprocessed blots are available in source data.

TCF3/TCF12 (Extended Data Fig. 10d-f). Notably, these mice were infertile (Fig. 5f). A detailed analysis showed ablation of Tcf3/Tcf12 led to a drastic loss of primordial follicles, with some progressing to a primary follicle-like state but not to the secondary follicles (Fig. 5c,d). To investigate the effect of TCF3/TCF12 deficiency on transcription, we manually performed single-oocyte RNA-seq for Tcf3/Tcf12 DKO oocytes at the GO-P10 stages (Fig. 6a). Uniform Manifold Approximation and Projection (UMAP) analysis showed that Tcf3/Tcf12 DKO oocytes were clustered closer to primordial follicles but were distinct from primary or secondary follicles in WT oocytes (Fig. 6a). To further pinpoint the states of these mutant oocytes, we identified stage-specific genes in oocytes from primordial, primary and secondary follicles. We also added RNA-seq data for PO oocytes in germ cell cysts isolated from newborn ovaries⁷² (Fig. 6a.b). Genes specifically activated in oocytes from primary and secondary follicles were expressed normally in Tcf3 or Tcf12 mKO oocytes, but completely failed to be expressed in *Tcf3/Tcf12* DKO oocytes (Fig. 6b). Therefore, despite some DKO oocytes morphologically resembling primary follicles (Fig. 5c,d), their transcriptomes were still arrested at the primordial follicle stage (Fig. 6b). The majority of primordial oocyte-specific genes were activated in DKO mutants. However, 20.1% (121 of 601) of them still failed to be expressed, including Zp1/Zp2/Zp3, Oas1c/Oas1d/Oas1e and Cnot7 (Fig. 6b, right). These data support compensatory functions between TCF3 and TCF12 and suggest that they, together, play key roles in oocyte development in primordial follicles, although we cannot fully exclude the possibility that they may also have different functions.

We then asked whether these transcription defects were related to TCF3/TCF12 binding. Among differentially expressed genes, the downregulated genes contained more TCF3/TCF12 motifs at their promoters (Fig. 6c). As attempts to profile the binding of TCF3/TCF12 in oocytes failed, we inferred TCF3/TCF12 binding sites based on ATAC-seq in GO-P7 (the earliest stage at which we could collect sufficient oocytes) and TCF3/TCF12 motifs using TOBIAS⁷³ (Fig. 6d, top and Methods). Encouragingly, the predicted TCF3/12 distal binding was also present near downregulated genes (Fig. 6d, bottom), as exemplified by that near Zp3, Tle6 and Nlrp5 (Fig. 6e). Zp3 and Tle6 were also bound by TCF3/TCF12 in mES cells^{69,74} (Fig. 6e). These downregulated genes in Tcf3/Tcf12 mutant oocytes significantly overlapped with the downregulated genes (Zp1/Zp2/Zp3, Oas1c/Oas1d/Oas1e, Tle6 and Npm2) in mouse oocytes deficient for Figla or Lhx8, two TFs required for primordial follicle formation or maintenance⁷⁵⁻⁷⁸ (Fig. 7a). Furthermore. TCF3 and TCF12 interacted with each other and both also interacted with FIGLA and LHX8 (Fig. 7b). As a negative control, TCF12 did not interact with FOXO3, another oocyte TF regulator⁷⁹. Thus, these data are in line with the notion that TCF3/TCF12 and FIGLA, LHX8 share common targets in oocytes. Immunostaining in the P2.5 ovary for TCF3, TCF12 and LHX8 (we did not find good antibodies for FIGLA) revealed that all three TFs exhibited nuclear localization and both TCF3 and TCF12 showed partial co-localization with LHX8 (Fig. 7c), supporting a model that they may function cooperatively. Taken together, these analyses revealed a drastic transition of the transcription factor network during the OET and identified TCF3/TCF12 as key regulators of mouse oogenesis.

Discussion

Transcription during mammalian gametogenesis and early development undergoes extensive reprogramming. However, the CREs underlying the transcription network in this process remain poorly understood. Here, we mapped putative enhancers across 15 stages during mouse oogenesis and embryogenesis. Our data demonstrate that the enhancer networks undergo drastic transition, bear unique epigenetic signatures and likely interact with stage-specific TFs to wire transcription networks in oocytes and early embryos (Fig. 7d).

Putative enhancers in oocytes and early embryos are globally distinct from those in tissues and cell lines (Fig. 1b). Many putative

enhancers appear in gene-poor regions in oocytes, where a number of oocyte-specific genes reside. The activities of these enhancers gradually diminish after fertilization. Notably, this correlated with loss of LADs in mouse FGOs and their subsequent re-establishment after fertilization²². It is tempting to speculate that loss of LADs in FGOs may enable an active transcription environment in gene deserts to permit the expression of a subset of oocyte-specific genes that are otherwise repressed. In mouse oocytes and pre-implantation embryos, many putative enhancers are also marked by H3K4me3, a classic promoter mark, likely due to DNA hypomethylation in the genomes (Fig. 4a), as observed in zebrafish *dnmt1*-deficient embryos³⁷. These data are consistent with the H3K4me3-H3K4me1 seesaw model previously proposed⁸⁰. In addition, H3K4me3 at enhancers is actively converted to H3K4me1 by the demethylases KDM5B/KDM5C in mES cells to avoid overactivation^{52,81}. Kdm5a/Kdm5b/Kdm5c are lowly expressed in FGOs⁸², which may further contribute to the widespread presence of H3K4me3 on enhancers. Future works are warranted to decipher the function of H3K4me3 at enhancers in oocytes and early embryos.

Earlier studies reported a lack of enhancer activities in oocytes ^{23,24}. Here, our study presented evidence of enhancer activities in FGOs using STARR-seq⁵³ and an enhancer reporter assay (Fig. 4d–g and Extended Data Fig. 9a–e). We noticed that at least for one enhancer tested previously²³, the corresponding TF (SP1) is poorly expressed in oocytes (Extended Data Fig. 10g). Moreover, our results indicate that the association of Pol II and CAGE signals may provide additional prediction power for active enhancers in oocytes than H3K27ac alone. Finally, in strong support of the notion that enhancers are actively employed in oocytes and early embryos, we identified key TF regulators of ovarian folliculogenesis, TCF3 and TCF12, inferred from the enhancer maps. Therefore, uncovering these regulatory networks represents an important step towards decoding the genetic circuitry underlying the OET, which resets the life clock to generate a totipotent embryo.

Online content

Any methods, additional references, Nature Portfolio reporting summaries, source data, extended data, supplementary information, acknowledgements, peer review information; details of author contributions and competing interests; and statements of data and code availability are available at https://doi.org/10.1038/s41556-024-01422-x.

References

- Long, H. K., Prescott, S. L. & Wysocka, J. Ever-changing landscapes: transcriptional enhancers in development and evolution. Cell 167. 1170–1187 (2016).
- 2. Yu, M. & Ren, B. The three-dimensional organization of mammalian genomes. *Annu. Rev. Cell Dev. Biol.* **33**, 265–289 (2017).
- Spitz, F. & Furlong, E. E. Transcription factors: from enhancer binding to developmental control. *Nat. Rev. Genet.* 13, 613–626 (2012).
- 4. Calo, E. & Wysocka, J. Modification of enhancer chromatin: what, how, and why? *Mol. Cell* **49**, 825–837 (2013).
- Ong, C.-T. & Corces, V. G. Enhancer function: new insights into the regulation of tissue-specific gene expression. *Nat. Rev. Genet.* 12, 283–293 (2011).
- Shlyueva, D., Stampfel, G. & Stark, A. Transcriptional enhancers: from properties to genome-wide predictions. Nat. Rev. Genet. 15, 272–286 (2014).
- Creyghton, M. P. et al. Histone H3K27ac separates active from poised enhancers and predicts developmental state. *Proc. Natl Acad. Sci. USA* 107, 21931–21936 (2010).
- 8. Grunstein, M. Histone acetylation in chromatin structure and transcription. *Nature* **389**, 349–352 (1997).
- Guerrini, M. M., Oguchi, A., Suzuki, A. & Murakawa, Y. Cap analysis of gene expression (CAGE) and noncoding regulatory elements. Semin. Immunopathol. 44, 127–136 (2022).

- Andersson, R. & Sandelin, A. Determinants of enhancer and promoter activities of regulatory elements. *Nat. Rev. Genet.* 21, 71–87 (2020).
- Du, Z., Zhang, K. & Xie, W. Epigenetic reprogramming in early animal development. Cold Spring Harb. Perspect. Biol. 14, a039677 (2022).
- Eckersley-Maslin, M. A., Alda-Catalinas, C. & Reik, W. Dynamics of the epigenetic landscape during the maternal-to-zygotic transition. *Nat. Rev. Mol. Cell Biol.* 19, 436–450 (2018).
- Fu, X., Zhang, C. & Zhang, Y. Epigenetic regulation of mouse preimplantation embryo development. *Curr. Opin. Genet Dev.* 64, 13–20 (2020).
- Dahl, J. A. et al. Broad histone H3K4me3 domains in mouse oocytes modulate maternal-to-zygotic transition. *Nature* 537, 548–552 (2016).
- Liu, X. et al. Distinct features of H3K4me3 and H3K27me3 chromatin domains in pre-implantation embryos. *Nature* 537, 558–562 (2016).
- Zhang, B. et al. Allelic reprogramming of the histone modification H3K4me3 in early mammalian development. *Nature* 537, 553–557 (2016).
- Zheng, H. et al. Resetting epigenetic memory by reprogramming of histone modifications in mammals. *Mol. Cell* 63, 1066–1079 (2016).
- Inoue, A., Jiang, L., Lu, F. & Zhang, Y. Genomic imprinting of Xist by maternal H3K27me3. Genes Dev. 31, 1927–1932 (2017).
- Inoue, A., Jiang, L., Lu, F., Suzuki, T. & Zhang, Y. Maternal H3K27me3 controls DNA methylation-independent imprinting. Nature 547, 419–424 (2017).
- Harris, C. et al. Conversion of random X-inactivation to imprinted X-inactivation by maternal PRC2. eLife 8, e44258 (2019).
- van Steensel, B. & Belmont, A. S. Lamina-associated domains: links with chromosome architecture, heterochromatin, and gene repression. Cell 169, 780–791 (2017).
- 22. Borsos, M. et al. Genome-lamina interactions are established de novo in the early mouse embryo. *Nature* **569**, 729–733 (2019).
- Lawinger, P., Rastelli, L., Zhao, Z. & Majumder, S. Lack of enhancer function in mammals is unique to oocytes and fertilized eggs. *J. Biol. Chem.* 274, 8002–8011 (1999).
- Majumder, S., Zhao, Z., Kaneko, K. & DePamphilis, M. L. Developmental acquisition of enhancer function requires a unique coactivator activity. *EMBO J.* 16, 1721–1731 (1997).
- Kim, J. M., Liu, H., Tazaki, M., Nagata, M. & Aoki, F. Changes in histone acetylation during mouse oocyte meiosis. J. Cell Biol. 162, 37–46 (2003).
- Akiyama, T., Nagata, M. & Aoki, F. Inadequate histone deacetylation during oocyte meiosis causes aneuploidy and embryo death in mice. Proc. Natl Acad. Sci. USA 103, 7339–7344 (2006).
- 27. Wu, J. et al. The landscape of accessible chromatin in mammalian preimplantation embryos. *Nature* **534**, 652–657 (2016).
- 28. Xiang, Y. et al. Epigenomic analysis of gastrulation identifies a unique chromatin state for primed pluripotency. *Nat. Genet.* **52**, 95–105 (2020).
- 29. Wang, M., Chen, Z. & Zhang, Y. CBP/p300 and HDAC activities regulate H3K27 acetylation dynamics and zygotic genome activation in mouse preimplantation embryos. *EMBO J.* **41**, e112012 (2022).
- Consortium, E. P. An integrated encyclopedia of DNA elements in the human genome. *Nature* 489, 57–74 (2012).
- Veselovska, L. et al. Deep sequencing and de novo assembly of the mouse oocyte transcriptome define the contribution of transcription to the DNA methylation landscape. *Genome Biol.* 16, 209 (2015).
- 32. Paillisson, A. et al. Identification, characterization and metagenome analysis of oocyte-specific genes organized in clusters in the mouse genome. *BMC Genomics* **6**, 76 (2005).

- 33. Santenard, A. et al. Heterochromatin formation in the mouse embryo requires critical residues of the histone variant H3.3. *Nat. Cell Biol.* **12**, 853–862 (2010).
- 34. Liu, B. et al. The landscape of RNA Pol II binding reveals a stepwise transition during ZGA. *Nature* **587**, 139–144 (2020).
- Zenk, F. et al. Germ line-inherited H3K27me3 restricts enhancer function during maternal-to-zygotic transition. Science 357, 212–216 (2017).
- 36. Du, Z. et al. Polycomb group proteins regulate chromatin architecture in mouse oocytes and early embryos. *Mol. Cell* 77, 825–839 (2020).
- Wu, X. et al. Methylome inheritance and enhancer dememorization reset an epigenetic gate safeguarding embryonic programs. Sci. Adv. 7, eabl3858 (2021).
- Wang, L. et al. Programming and inheritance of parental DNA methylomes in mammals. Cell 157, 979–991 (2014).
- 39. Shirane, K. et al. Mouse oocyte methylomes at base resolution reveal genome-wide accumulation of non-CpG methylation and role of DNA methyltransferases. *PLoS Genet.* **9**, e1003439 (2013).
- Hanna, C. W. et al. MLL2 conveys transcription-independent H3K4 trimethylation in oocytes. Nat. Struct. Mol. Biol. 25, 73–82 (2018).
- 41. Smallwood, S. A. et al. Dynamic CpG island methylation landscape in oocytes and preimplantation embryos. *Nat. Genet.* **43**, 811–814 (2011).
- 42. Pekowska, A. et al. H3K4 tri-methylation provides an epigenetic signature of active enhancers. *EMBO J.* **30**, 4198–4210 (2011).
- The ENCODE Project Consortium et al. Expanded encyclopaedias of DNA elements in the human and mouse genomes. *Nature* 583, 699–710 (2020).
- 44. Lam, M. T., Li, W., Rosenfeld, M. G. & Glass, C. K. Enhancer RNAs and regulated transcriptional programs. *Trends Biochem. Sci.* **39**, 170–182 (2014).
- 45. Zhu, Y. et al. Predicting enhancer transcription and activity from chromatin modifications. *Nucleic Acids Res.* **41**, 10032–10043 (2013).
- 46. Yu, C. et al. TBPL2/TFIIA complex establishes the maternal transcriptome through oocyte-specific promoter usage. *Nat. Commun.* **11**, 6439 (2020).
- Haberle, V., Forrest, A. R., Hayashizaki, Y., Carninci, P. & Lenhard, B. CAGEr: precise TSS data retrieval and high-resolution promoterome mining for integrative analyses. *Nucleic Acids Res.* 43, e51 (2015).
- Thodberg, M., Thieffry, A., Vitting-Seerup, K., Andersson, R. & Sandelin, A. CAGEfightR: analysis of 5'-end data using R/Bioconductor. BMC Bioinform. 20, 487 (2019).
- 49. Shen, Y. et al. A map of the *cis*-regulatory sequences in the mouse genome. *Nature* **488**, 116–120 (2012).
- Shahbazian, M. D. & Grunstein, M. Functions of site-specific histone acetylation and deacetylation. *Annu. Rev. Biochem.* 76, 75–100 (2007).
- Dahlin, J. L. et al. Assay interference and off-target liabilities of reported histone acetyltransferase inhibitors. *Nat. Commun.* 8, 1527 (2017).
- 52. Shen, H. et al. Suppression of enhancer overactivation by a RACK7-Histone demethylase complex. *Cell* **165**, 331–342 (2016).
- 53. Neumayr, C., Pagani, M., Stark, A. & Arnold, C. D. STARR-seq and UMI-STARR-seq: assessing enhancer activities for genome-wide, high-, and low-complexity candidate libraries. *Curr. Protoc. Mol. Biol.* **128**, e105 (2019).
- 54. Picelli, S. et al. Smart-seq2 for sensitive full-length transcriptome profiling in single cells. *Nat. Methods* **10**, 1096–1098 (2013).
- 55. Lee, D. et al. STARRPeaker: uniform processing and accurate identification of STARR-seq active regions. *Genome Biol.* **21**, 298 (2020)
- 56. Klein, J. C. et al. A systematic evaluation of the design and context dependencies of massively parallel reporter assays. *Nat. Methods* **17**, 1083–1091 (2020).

- Heinz, S. et al. Simple combinations of lineage-determining transcription factors prime cis-regulatory elements required for macrophage and B cell identities. Mol. Cell 38, 576–589 (2010).
- Whiddon, J. L., Langford, A. T., Wong, C.-J., Zhong, J. W. & Tapscott, S. J. Conservation and innovation in the DUX4-family gene network. *Nat. Genet.* 49, 935–940 (2017).
- Hendrickson, P. G. et al. Conserved roles of mouse DUX and human DUX4 in activating cleavage-stage genes and MERVL/ HERVL retrotransposons. Nat. Genet. 49, 925–934 (2017).
- De Iaco, A. et al. DUX-family transcription factors regulate zygotic genome activation in placental mammals. *Nat. Genet.* 49, 941–945 (2017).
- Ji, S. et al. OBOX regulates mouse zygotic genome activation and early development. *Nature* 620, 1047–1053 (2023).
- Youjia, G. et al. Obox4 promotes zygotic genome activation upon loss of Dux. Preprint at bioRxiv https://doi.org/10.1101/2022. 07.04.498763 (2024).
- Lai, F. et al. NR5A2 connects zygotic genome activation to the first lineage segregation in totipotent embryos. *Cell Res.* 33, 952–966 (2023).
- 64. Festuccia, N. et al. Nr5a2 is essential for morula development. Preprint at bioRxiv https://doi.org/10.1101/2023.01.16.524255 (2023).
- 65. Gassler, J. et al. Zygotic genome activation by the totipotency pioneer factor Nr5a2. Science **378**, 1305–1315 (2022).
- Jones, M. E. & Zhuang, Y. Acquisition of a functional T cell receptor during T lymphocyte development is enforced by HEB and E2A transcription factors. *Immunity* 27, 860–870 (2007).
- 67. Barndt, R. J., Dai, M. & Zhuang, Y. Functions of E2A-HEB heterodimers in T-cell development revealed by a dominant negative mutation of HEB. *Mol. Cell. Biol.* **20**, 6677–6685 (2000).
- Zhuang, Y., Barndt, R. J., Pan, L., Kelley, R. & Dai, M. Functional replacement of the mouse E2A gene with a human HEB cDNA. Mol. Cell. Biol. 18, 3340–3349 (1998).
- Yoon, S. J., Foley, J. W. & Baker, J. C. HEB associates with PRC2 and SMAD2/3 to regulate developmental fates. *Nat. Commun.* 6, 6546 (2015).
- Liang, L. F., Soyal, S. M. & Dean, J. FIG alpha, a germ cell specific transcription factor involved in the coordinate expression of the zona pellucida genes. *Development* 124, 4939–4947 (1997).
- Lim, E. J. & Choi, Y. Transcription factors in the maintenance and survival of primordial follicles. *Clin. Exp. Reprod. Med.* 39, 127–131 (2012).
- He, Y. et al. Single-cell RNA-Seq reveals a highly coordinated transcriptional program in mouse germ cells during primordial follicle formation. Aging Cell 20, e13424 (2021).

- 73. Bentsen, M. et al. ATAC-seq footprinting unravels kinetics of transcription factor binding during zygotic genome activation. *Nat. Commun.* **11**, 4267 (2020).
- 74. Wang, Q. et al. The p53 family coordinates Wnt and nodal inputs in mesendodermal differentiation of embryonic stem cells. *Cell Stem Cell* **20**, 70–86 (2017).
- Choi, Y., Ballow, D. J., Xin, Y. & Rajkovic, A. Lim homeobox gene, Lhx8, is essential for mouse oocyte differentiation and survival1. *Biol. Reprod.* 79, 442–449 (2008).
- D'Ignazio, L. et al. Lhx8 ablation leads to massive autophagy of mouse oocytes associated with DNA damage. *Biol. Reprod.* 98, 532–542 (2018).
- Soyal, S. M., Amleh, A. & Dean, J. FIGα, a germ cell-specific transcription factor required for ovarian follicle formation. Development 127, 4645–4654 (2000).
- 78. Wang, Z., Liu, C. Y., Zhao, Y. & Dean, J. FIGLA, LHX8 and SOHLH1 transcription factor networks regulate mouse oocyte growth and differentiation. *Nucleic Acids Res.* **48**, 3525–3541 (2020).
- John, G. B., Gallardo, T. D., Shirley, L. J. & Castrillon, D. H. Foxo3 is a PI3K-dependent molecular switch controlling the initiation of oocyte growth. *Dev. Biol.* 321, 197–204 (2008).
- 80. Sharifi-Zarchi, A. et al. DNA methylation regulates discrimination of enhancers from promoters through a H3K4me1-H3K4me3 seesaw mechanism. *BMC Genomics* **18**, 964 (2017).
- 81. Kidder, B. L., Hu, G. & Zhao, K. KDM5B focuses H3K4 methylation near promoters and enhancers during embryonic stem cell self-renewal and differentiation. *Genome Biol.* **15**, R32 (2014).
- 82. Shao, G. B. et al. Dynamic patterns of histone H3 lysine 4 methyltransferases and demethylases during mouse preimplantation development. *Vitr. Cell Dev. Biol. Anim.* **50**, 603–613 (2014).

Publisher's note Springer Nature remains neutral with regard to jurisdictional claims in published maps and institutional affiliations.

Springer Nature or its licensor (e.g. a society or other partner) holds exclusive rights to this article under a publishing agreement with the author(s) or other rightsholder(s); author self-archiving of the accepted manuscript version of this article is solely governed by the terms of such publishing agreement and applicable law.

@ The Author(s), under exclusive licence to Springer Nature Limited 2024

¹Center for Stem Cell Biology and Regenerative Medicine, MOE Key Laboratory of Bioinformatics, New Cornerstone Science Laboratory, School of Life Sciences, Tsinghua University, Beijing, China. ²Tsinghua-Peking Center for Life Sciences, Beijing, China. ³State Key Laboratory of Reproductive Medicine and Offspring Health, Nanjing Medical University, Nanjing, China. ⁴Innovation Center of Suzhou Nanjing Medical University, Suzhou, China. ⁵Laboratory of Molecular Developmental Biology, State Key Laboratory of Membrane Biology, Tsinghua University, Beijing, China. ⁵Institute of Epigenetics and Stem Cells (IES), Helmholtz Zentrum München, Munich, Germany. ¹Center for Stem Cell Biology and Regenerative Medicine, School of Medicine, Tsinghua University, Beijing, China. ⁵These authors contributed equally: Bofeng Liu, Yuanlin He, Xiaotong Wu, Zili Lin, Jing Ma. ⊠e-mail: ljwth@njmu.edu.cn; xiewei121@tsinghua.edu.cn

Methods

Animal maintenance

All animal maintenance and experimental procedures were carried out according to the Institutional Animal Care and Use Committee guidelines of Tsinghua University, Beijing, China or under the authorization of the Upper Bavarian Government (ethical approval protocol no. 21-XW2 and IACUC-1601220). All oocytes were collected from WT C57BL/6N females. PWK/PhJ mice were originally purchased from The Jackson Laboratory and raised in the local core facility. C57BL/6 and ICR mice were purchased from Vital River.

Preparation of mouse oocytes and embryos

In brief, GOs were isolated by mechanical dissection in M2 medium (Sigma, M7167). GOs were isolated from mice at postnatal day 7 or day 10. Pre-implantation embryos were collected from 5–6-week-old C57BL/6N females (Vital River) mated with PWK/PhJ males (The Jackson Laboratory). Adult female mice were superovulated for oocyte and embryo collection. For superovulation, female mice were injected intraperitoneally with 7.5 IU pregnant mare serum gonadotropin (PMSG) and human chorionic gonadotropin (hCG) with 5 IU 46–48 h after PMSG injection. FGOs (>70 μ m) were isolated from 8-week-old mice 46–48 h after PMSG injection. MII oocytes were isolated from 6-week-old mice 20 h after hCG injection. Each set of embryos was isolated at a defined period after hCG injection, 27–29 h (PN5 zygotes), 33–35 h (early two-cell), 46–48 h (late two-cell), 62–65 h (eight-cell), 94–96 h (blastocysts) in M2 medium.

At least 200 cells were collected for STAR ChIP-seq experiments. To remove the granulosa cells, the dissociated oocyte and granulosa cell complexes were transferred into M2 medium containing 0.1% hyaluronidase (Sigma, A5177) and digested for 5 min. Oocytes were collected after removing the zona pellucida by acidic Tyrode's solution (Sigma, T1788) treatment. To remove the zona pellucida of embryos, the embryos were incubated with 10 IU ml⁻¹ pronase (Sigma, P8811) for several minutes. Samples were washed in PBS quickly and manually picked up into the lysis buffer (0.5% NP-40, 0.5% Tween-20, 0.1% SDS and proteinase inhibitor) for STAR ChIP-seq.

Cell culture of ES cells

The R1 ES cells were cultured on gelatin in DMEM containing 15% FBS, leukaemia inhibiting factor, penicillin/streptomycin, L-glutamine, β -mercaptoethanol and non-essential amino acids.

STAR ChIP-seq library preparation and sequencing

STAR ChIP-seq library preparation was conducted following a protocol described previously16. In brief, each sample was subjected to MNase (Sigma, N3755-200UN) digestion at 37 °C. The reaction was terminated by adding stop buffer (110 mM Tris-HCl, pH 8.0 and 55 mM EDTA) and cold 2× RIPA buffer. Each chromatin sample was supplemented with RIPA buffer to make sure the lipid in the tube could flow while rotating it. The IP sample was incubated with antibodies for H3K27ac (Active Motif, 39133, 1:70 diluted) overnight with rotation at 4 °C. The next day, the sample was incubated with protein A Dynabeads (Life Technologies) for 2 h with rotation at 4 °C. Beads were washed with RIPA buffer four times and LiCl buffer once. After washing, tubes were spun briefly and the supernatant was removed. For each IP sample, beads were resuspended with ddH₂O and Ex-Taq buffer (TaKaRa). Then, 1 µl proteinase K (Roche, 10910000) was added at 55 °C for 90 min to elute DNA from beads. The supernatant was transferred to a new tube and the proteinase K was inactivated at 72 °C for 40 min. Then, 1 µl rSAP (NEB, M0371) was added to dephosphorylate the 3' end of DNA at 37 °C for 1 h. rSAP was inactivated at 65 °C for 10 min. The resulting sample was subjected to library preparation starting from PolyC tailing as previously described83. Mouse sperm ChIP-seq was performed as described previously with modifications84.

Whole-mount immunofluorescent staining

Oocytes and embryos were fixed in 4% paraformaldehyde at room temperature for 30 min. Subsequently, they were permeabilized for 10 min in PBST (1% Triton X-100). After blocking with 1% BSA for 1 h, samples were incubated with H3K27ac antibody (Active Motif, 39133, 1:200 diluted) at 4 °C overnight. The secondary antibody Alexa Fluor 488-conjugated anti-rabbit (Jackson ImmunoResearch, 611-545-215, 1:200 diluted) was added with 4,6-diamidino-2-phenylindole (DAPI) (Invitrogen, D1306) after washing the primary antibody. Images were acquired on an 880 META laser scanning confocal microscope and manipulated by ZEN software (v.3.9).

DamID library preparation and sequencing

The DamID procedure was performed as previously described 22 . In brief, a messenger RNA mixture containing 100 ng μl^{-1} membrane-eGFP and AID–Dam-lamin B1 or AID–Dam were injected into the cytoplasm of oocytes. Oocytes were isolated and injected with 5 ng μl^{-1} AID–Dam-lamin B1 or 20 ng μl^{-1} AID–Dam and kept in auxin-free M2 medium for 6–8 h to methylate LADs or accessible regions, respectively. Following oocyte collection, library preparation and sequencing were performed as previously described 22 .

Inhibitor treatment

To block H3K27ac, FGOs were collected and cultured in M2 medium containing 60 μ M plumbagin (Selleck, S4777) for 24 h with milrinone. FGOs cultured in M2 medium with 0.1% DMSO were used as control.

EU staining

Cell-LightTM EU Nascent RNA Detection kit (RiboBIO, C10316) was used to explore the transcription level of Plumbagin or DMSO-treated FGOs. These FGOs were transferred into 100 μ l 500 mMEU solution (1:1,000 diluted in medium), soaked at 37 °C for 2 h, washed several times with PBS (GIBCO, 21600-044) and fixed by 4% polyformaldehyde for 30 min at room temperature. FGOs were permeabilized with 1% PBST at room temperature for 10 min and washed with PBS several times before staining in 100 μ l Apollo reaction buffer (Apollo 567 nm). Freshly prepared Apollo reaction buffer was maintained in the dark for 30 min at room temperature with gentle shaking, after which DNA-stained embryos with DAPI were mounted and imaged using an 880 META laser scanning confocal microscope.

STARR-seq plasmid library cloning

The candidate enhancer sequences were obtained from PCR of genome DNA (primer sequences in Supplementary Table 3) and cloned between the truncated form of GFP and the polyA site in the hSTARR-seq ORI vector (Addgene, #99296). Purified PCR products of each candidate enhancer were pooled together and ligated with Illumina adaptors in DNA Library Prep kit (NEB, E7645S). Subsequently, adaptor-ligated PCR products were purified with AMPure XP beads and amplificated by PCR with library cloning primers (forward: 5'-TAGAGCATGCACCGGACACTCTTTCCCTA-CACGACGCTCTTCCGATCT, reverse: 5'-GGCCGAATTCGTCGAGT-GACTGGAGTTCAGACGTGTGCTCTTCCGATCT) (1 µl adaptor-ligated PCR products, 2.5 µl 10 µM forward primer, 2.5 µl 10 µM reverse primer, 25 µl KAPA 2× HiFi HotStart Ready Mix (Roche, KK2602) and 19 µl H₂O) with the programme of 98 °C for 45 s (98 °C for 15 s, 65 °C for 30 s and 72 °C for 45 s) with five cycles and 72 °C for 2 min, which results in that candidate sequences were flanked by overlap sequences with vector around insertion site. The hSTARR-seq_ORI vector was restriction digested by Agel-HF and Sall-HF and purified for Gibson assembly with ClonExpress II One Step Cloning kit (Vazyme, C112). The STARR-seq plasmid library was amplified using Illumina i5 and i7 index primers and its quality and complexity were assessed by deep sequencing.

STARR-seq library preparation and sequencing

The STARR-seq plasmid library was purified and injected into the pronucleus of FGOs cultured with milrinone. After 24 h, the FGOs were lysed in hypotonic lysis buffer (Vazyme, N712) and the polyadenylated mRNAs were captured by the oligonucleotide (dT) primers. After 3 min at 72 °C, the Smart-seq2 reverse transcription reactions were performed. After pre-amplification and AMPure XP beads purification, cDNAs were amplified with junction PCR primers (forward: 5′-TCGTGAGGCACTGGC CAG*G*T*G*T*C, reverse: 5′-CTTATCATGTCTGCTCGA*A*G*C, where * indicates a phosphorothioate bond), which specifically enriches reporter transcripts and excludes STARR-seq plasmids. Then the PCR products were cleaned up with AMPure XP beads and we performed sequencing-ready PCR to add Illumina i5 and i7 indexes for deep sequencing. All libraries were sequenced on an Illumina HiSeq 2500 platform.

Oocyte reporter assay

The hSTARR-seq_ORI vector (Addgene, #99296) was modified for reporter assay constructs: truncated *Gfp* was replaced with a *mNeon-Green* coding sequence. Candidate enhancer sequences were inserted after polyA. The primer sequences used for the amplification of candidate enhancers are listed in Supplementary Table 2. *Zp3* promoter was inserted into the pGL4.23 luciferase reporter vector (Promega, E8411) and the luciferase gene was replaced with an *mCherry* coding sequence, which acts as a control for enhancer reporter. Purified enhancer reporter plasmid for each candidate enhancer and *Zp3-mCherry* plasmid were injected into the pronucleus of FGOs cultured with milrinone. After 24 h, the ratio of mNeonGreen to mCherry fluorescence intensity was recorded as enhancer activity.

Tcf3/Tcf12 and Eed cKO mice

 $Tcf3^{flox/flox}$ and $Tcf12^{flox/flox}$ transgenic mice were gifted from Y. Zhuang at Duke University. Gdf9-Cre mice were gifted from Y. Su at Shandong University. The Gdf9-Cre mice were crossed with $Tcf3^{flox/flox}$ and $Tcf12^{flox/flox}$ mice to establish Gdf9-Cre $Tcf3^{flox/flox}$ $Tcf12^{flox/flox}$ cKO mice. All mice had a C57BL/6J genetic background. Primers used for genotyping are listed in Supplementary Table 1. Eed KO mice were previously described 36 . In brief, $Eed^{flox/flox}$ FGOs and Eed^{-f-} FGOs were collected from 8-week-old $Eed^{flox/flox}$ and $Eed^{flox/flox}$ Gdf9-Cre mice, respectively.

H&E staining, **IHC and IF staining**

Ovaries were fixed in 10% formalin overnight, paraffin-embedded and sectioned to a thickness of 5 μ m. Sections were deparaffinized and rehydrated and endogenous peroxidase activity was blocked by incubating in 3% hydrogen peroxide in methanol for 15 min.

The sections were stained with H&E. Follicles were classified as primordial follicles (an oocyte surrounded by a partial or complete layer of squamous granulosa cells), primary follicles (a single layer of cuboidal granulosa cells), secondary follicles (more than one layer of cuboidal granulosa cells with nonvisible antrum) and antral follicles (a clearly defined antral space and a cumulus granulosa cell layer).

For immunohistochemistry (IHC), the antigen of ovarian sections was retrieved at 95 °C for 15 min in 10 mM sodium citrate buffer (pH 6.0). Sections were blocked for 60 min at room temperature in PBS contained with 5% BSA and incubated at 4 °C overnight with the primary antibodies: TCF3 (Proteintech, 21242-1-AP, 1:200 dilution) and TCF12 (Proteintech, 14419-1-AP, 1:200 dilution). Subsequently, the sections were washed with TBS 5 min three times and incubated with secondary antibodies for 60 min. The signals were coloured with a diaminobenzidine (DAB) reagent (ZSGB-BIO).

Immunofluorescence (IF) staining was performed with a multi-immunofluorescent kit (Aifang Biological, AFIHC033). Samples were incubated with primary antibodies: TCF3 (Proteintech, 21242-1-AP, 1:2,000 diluted), TCF12 (Proteintech, 14419-1-AP, 1:2,000 diluted) and LHX8 (Abclonal, A2046, 1:2,000 diluted).

Quantitative real-time PCR

The method for preparing cDNA was adapted from the Smart-seq2 protocol 54 . qPCR was performed using the ChamQ SYBR Green qPCR Master Mix (Vazyme Q311) with an ABI StepOnePlus Real-Time PCR system (Applied Biosystems, Life Technologies). Relative mRNA levels were calculated by normalizing them to β -Actin mRNA levels. Primer sequences are listed in Supplementary Table 1.

Western blot

Ovaries were lysed in RIPA (Beyotime Institute of Biotechnology, P0013B) with 1% protease inhibitor (MCE, HY-K0012). Proteins were separated by electrophoresis by 10% SDS–PAGE and transferred into polyvinylidene fluoride membranes (Bio-Rad). The membranes were blocked with 5% nonfat dry milk for 60 min and incubated at 4 °C overnight with the following primary antibodies: TCF3 (Proteintech, 21242-1-AP, 1:800 diluted), TCF12 (Proteintech, 14419-1-AP, 1:800 diluted) and β -tubulin (Yifei Xue Biotechnology, YFMA0053, 1:1,000 diluted). The membranes were washed with TBST for 10 min three times and incubated with secondary antibodies for 60 min. The signals were enhanced through enhanced chemiluminescence (Biosharp, BL520A).

RNA-seq library preparation and sequencing for oocytes

The ovaries were digested in 500 μ l HBSS supplemented with 0.25% trypsin, 1 mM EDTA and 0.01% DNase I and incubated at 37 °C for 10 min with gentle agitation. After aspirating the supernatant completely, the cells were resuspended in 500 μ l HBSS. The dissociated single-cell suspensions were transferred under the microscope (Nikon, SMZ1000) and oocytes were washed three times with 0.1% BSA/PBS, each oocyte was transferred into 0.2-ml PCR tubes containing 2 μ l lysis buffer. Transcriptome libraries were prepared following the Smart-seq2 protocol S4. Sequencing libraries were constructed by using KAPA HyperPlus kit (Kapa Biosystems) according to the manufacturer's instructions. All libraries were sequenced on the Illumina NovaSeq 6,000 platform.

ATAC-seq library preparation and sequencing

The ATAC-seq procedure was performed as previously described 27 . In brief, cells were transferred into 6 μ l lysis buffer (10 mM Tris-HCl, pH 7.4, 10 mM NaCl, 3 mM MgCl $_2$ and 0.5% NP-40) on ice for 10 min. The ATAC reaction was performed by adding 4 μ l ddH $_2$ O, 4 μ l 5× TTBL and 5 μ l TTE mix V5 (Vazyme, TD502) at 37 °C for 30 min and then stopped by adding 5 μ l 5× TS stop buffer at room temperature for 5 min. The DNA product was PCR-amplified with 10 μ l index (Vazyme, TD202), 10 μ l 5× TAB and 1 μ l TAE (Vazyme, TD502) for 16 cycles. The amplified DNA was size-selected using AMPure Beads for 200–800-bp DNA fragments. All libraries were sequenced by an Illumina 2500 or XTen platform, accordingly.

Data analyses

ChIP-seq data processing. The paired-end reads were aligned with the parameters: -t -q -N 1 -L 25 -X 2,000-no-mixed-no-discordant by Bowtie (v.2.2.2)85. All unmapped reads, non-uniquely mapped reads and PCR duplicates were removed. For downstream analysis, we normalized the read counts by computing the numbers of reads per kilobase of bin per million of reads sequenced (RPKM). RPKM values were calculated by merged replicate bam files (SAMtools v.1.3.1)86. To minimize the batch and cell-type variation, the RPKM values were further normalized through z-score transformation (Python v.2.7.12). To visualize the ChIP-seq signal in the UCSC genome browser, we extended each read by 250 bp and counted the coverage for each base (bedGraphToBigWig v.4). The correlation between ChIP-seq replicates was calculated as follows: ChIP-seq correlation was calculated by deep-Tools⁸⁷. Allele assignment of sequencing reads for mouse embryos was conducted as described previously²⁷. The distal H3K27ac peaks (beyond ±2.5 kb from TSSs) were identified as putative enhancers (Supplementary Table 4).

Gene expression data processing. All RNA-seq data were mapped to mm9 genome by Tophat $(v.2.4.0)^{88}$. The gene expression level was calculated by Cufflinks $(v.2.2.1)^{88}$ based on the annotation mm9 refFlat database from the UCSC genome browser. The expression matrix (FPKM) for control and Tcf3/Tcf12 DKO single-oocyte RNA-seq was produced in a manner similarly to that of bulk RNA-seq data. Subsequently, the data were imported into Seurat $(v.4.2.1)^{89}$ to perform UMAP clustering and compute the average expression.

DNase-seq, ATAC-seq, DNA methylation, DamID and STARR-seq data processing. DNase-seq and ATAC-seq were mapped to mm9 genome by Bowtie with similar parameters as ChIP-seq data. For downstream analysis, we calculated the read counts by computing RPKM on the genome 100-bp bin. DNA methylation data were mapped to mm9 genome by BSMAP (v.2.74)⁹⁰ with parameters: -r 0-p 16-w 100-v 0.1. PCR duplicates were removed. For each CG site, the methylation level was calculated as the total methylated counts (combining Watson and Crick strands) divided by the total counts across all reads covering this CG.

DamID was processed as previously described²². In brief, DamID was mapped to the mm10 genome and the computation of OE values per bin was carried out as previously described²¹. Reads that precisely flanked an annotated GATC site were associated with GATC fragments and kept for downstream analysis.

STARR-seq was processed as previously described⁵³. In brief, STARR-seq was mapped to the mm9 genome by Bowtie with similar parameters as ChIP-seq data. For downstream analysis, we calculated the read counts by computing RPKM on the genome 100-bp bin for input controls and RNA. STARR-seq signals were then calculated as RNA/input. The background level of STARR-seq was estimated using all negative controls (n = 64; 16 negative controls × two replicates × both strands). After excluding outliers (n = 4), the background cutoff was determined as the values that correspond to mean + 3 × s.d. (fold change = 0.29, 99.7% confidence level). Enhancer candidates with STARR-seq RNA/input higher than the background cutoff in both replicates from at least one strand of enhancers were identified as STARR-seq-positive enhancers. The rest were classified as STARR-seq-negative enhancers.

Analyses of ChIP-seq peaks and peak comparison. H3K27ac peaks were called using HOMER⁵⁷ with the parameters -region -size 1,000 -minDist 1,500 -gsize 2.9×10^9 -fdr 0.0005. The peaks with tag count numbers more than 40 were selected as strong peaks for downstream analysis. Peak comparison was conducted using BEDTools (v.2.26.0)⁹² intersectBed function.

Identification of stage-specific genes. A Shannon-entropy-based method was used to identify stage-specific genes, as previously described⁹³. Genes with entropy score less than 2 were selected as candidates for stage-specific genes. Among these genes, we selected candidates of stage-specific genes for each stage based on the following criteria: the gene is highly expressed at this stage (FPKM > 5) and such high expression cannot be observed in more than two additional stages. These genes were then reported in the final stage-specific gene lists and visualized using Java TreeView (v.1.1.6r4)⁹⁴.

The comparison between H3K27ac ChIP-seq peaks and repetitive elements. To identify the enrichment of repetitive elements in distal H3K27ac peaks, the ChIP-seq peaks were compared with the locations of annotated repeats (RepeatMasker) downloaded from the UCSC genome browser. As repeats of different classes vary greatly in numbers, a random set of peaks with identical lengths of ChIP-seq peaks were used for the same analysis as a control. The numbers of observed peaks that overlap with repeats were compared with the number of random peaks that overlap with repeats and a log ratio value (log₂) was generated as the 'observed/expected' enrichment.

Motif analyses for distal H3K27ac ChIP-seq peaks. To find the sequence motif enriched in ChIP-seq peaks, findMotifsGenome.pl from the HOMER program was used⁵⁷.

Gene Ontology analysis. The DAVID web-tool (v.6.8) ⁹⁵ was employed to identify the Gene Ontology terms using databases including molecular functions, biological functions and cellular components ⁹⁶.

Hierarchical clustering analysis. Hierarchical clustering was performed in R (v.4.2.1) by hclust() function with ChIP-seq RPKM values via Pearson correlation coefficients.

Identification of oocyte enhancers by CAGE. The GO-P14 oocytes GAGE data were obtained from previous work⁴⁶ and mapped to mm9 genome using Bowtie (v.2.2.2)⁸⁵. Uniquely mapped reads were kept for downstream analyses using CAGEr Bioconductor package⁴⁷. The unidirectional and bidirectional transcription starting sites were identified using CAGEfightR⁴⁸. The candidate enhancers identified by CAGE in GO-P14 are included in Supplementary Table 5.

Statistical analyses and reproducibility. Statistical analyses were performed in GraphPad Prism v.8.2.0 and R v.4.2.1. No statistical methods were used to predetermine sample size. No data were excluded from the analyses. The experiments were not randomized and the investigators were not blinded to allocation during outcome assessment.

Reporting summary

Further information on research design is available in the Nature Portfolio Reporting Summary linked to this article.

Data availability

The generated and analysed data are available in the Gene Expression Omnibus with accession number GSE217970. Source data are provided with this paper.

References

- Peng, X. et al. TELP, a sensitive and versatile library construction method for next-generation sequencing. *Nucleic Acids Res.* 43, e35 (2015).
- 84. Hisano, M. et al. Genome-wide chromatin analysis in mature mouse and human spermatozoa. *Nat. Protoc.* **8**, 2449–2470 (2013).
- 85. Langmead, B. & Salzberg, S. L. Fast gapped-read alignment with Bowtie 2. *Nat. Methods* **9**, 357–359 (2012).
- 86. Danecek, P. et al. Twelve years of SAMtools and BCFtools. *Gigascience* **10**, giab008 (2021).
- 87. Ramirez, F. et al. deepTools2: a next generation web server for deep-sequencing data analysis. *Nucleic Acids Res.* **44**, W160–W165 (2016).
- 88. Trapnell, C. et al. Differential gene and transcript expression analysis of RNA-seq experiments with TopHat and Cufflinks. *Nat. Protoc.* **7**, 562–578 (2012).
- 89. Hao, Y. et al. Integrated analysis of multimodal single-cell data. *Cell* **184**, 3573–3587 (2021).
- 90. Xi, Y. & Li, W. BSMAP: whole genome bisulfite sequence MAPping program. *BMC Bioinform.* **10**, 232 (2009).
- 91. Kind, J. et al. Genome-wide maps of nuclear lamina interactions in single human cells. *Cell* **163**, 134–147 (2015).
- 92. Quinlan, A. R. BEDTools: the Swiss-army tool for genome feature analysis. *Curr. Protoc. Bioinform.* **47**, 11.12.1–11.12.34 (2014).
- Schug, J. et al. Promoter features related to tissue specificity as measured by Shannon entropy. *Genome Biol.* 6, R33 (2005).
- Saldanha, A. J. Java Treeview–extensible visualization of microarray data. *Bioinformatics* 20, 3246–3248 (2004).

- 95. Huang, D. W., Sherman, B. T. & Lempicki, R. A. Systematic and integrative analysis of large gene lists using DAVID bioinformatics resources. *Nat. Protoc.* **4**, 44–57 (2009).
- Dennis, G. Jr et al. DAVID: database for annotation, visualization, and integrated discovery. Genome Biol. 4. P3 (2003).
- 97. Lin, S. et al. Comparison of the transcriptional landscapes between human and mouse tissues. *Proc. Natl Acad. Sci. USA* 111, 17224–17229 (2014).
- Xiong, Z. et al. Ultrasensitive Ribo-seq reveals translational landscapes during mammalian oocyte-to-embryo transition and pre-implantation development. *Nat. Cell Biol.* 24, 968–980 (2022).

Acknowledgements

We are grateful to members of the Xie laboratory and the Li laboratory for the discussion and comments during the preparation of the manuscript and the Animal Center and Biocomputing Facility at Tsinghua University for their support. We thank X. Hu, L. Li, L. Wang, X. Lu, Q. Xu, Z. Du, Y. Zhang, G. Yu, H. Zheng, L. Liu and Y. Li for the help of various experiments and bioinformatics analyses. We are indebted to F. Lan, D. Fang and A. Stark for offering reagents or insightful discussion. We are grateful to Y. Zhuang for the $\mathit{Tcf3}^{\mathsf{flox/flox}}$ and Tcf12^{flox/flox} transgenic mice and Y. Su for the Gdf9-Cre mice. This work was funded by the National Natural Science Foundation of China (31988101 to W. Xie), the National Key R&D Program of China (2021YFA1100102 and 2019YFA0508900 to W. Xie, 2022YFC2703000 to J.L. and 2023YFA1800300 to X.W.), the National Natural Science Foundation of China (31830047 and 31725018 to W. Xie) and the Tsinghua-Peking Center for Life Sciences (W. Xie). B.L. is supported by Tsinghua Shuimu Scholar and Center for Life Sciences postdoctoral fellowship. W. Xie is a recipient of an HHMI International Research Scholar award and is a New Cornerstone Investigator.

Author contributions

W. Xie and J.L. conceived and designed the project. Z.L., F.K., P.W., J. Ming, F.L. and J. Ma collected and prepared WT and *Eed* KO embryos and oocytes. Y.H. and Y.Q. collected *Tcf3/12* DKO, *Tcf3* mKO and *Tcf12*

mKO oocytes. J. Ma, B.L., Y.X. and B.Z. conducted STAR ChIP-seg in mouse oocytes, embryos and mES cells, B.L. conducted ATAC-seg in mouse oocytes. X.W. modified and conducted STARR-seq in mouse oocytes with the help of W.S. Y.H. conducted single-oocyte RNA-seg. X.W. and Y.Q. conducted immunostaining in WT oocytes and embryos with the help of Z.L. and P.W. X.W. conducted plumbagin treatment, EU staining and reporter assay in FGOs with the help of F.K., F.L. and Z.L. F.K., Z.L. and F.L. conducted microinjection in oocytes. Y.Q. conducted qPCR, western blot, IHC, H&E staining in Tcf3/12 DKO oocytes and IP in HEK293T cells. Y.Q. analysed fertility and follicle numbers of Tcf3/12 DKO, Tcf3 mKO and Tcf12 mKO mice. Q.W. prepared Dnmt3a/b^{-/-} mES cells. M.P. and M.-E.T.-P. conducted lamin B1 DamID. W. Xia helped with various experiments. B.L. conducted the bioinformatics analysis with the help of J.W., B.Z. and Y.X. B.L., X.W. and W. Xie prepared most figures and wrote the manuscript with help of J.L., Y.Q., M.-E.T.-P., M.P., J.N. and all other authors.

Competing interests

The authors declare no competing interests.

Additional information

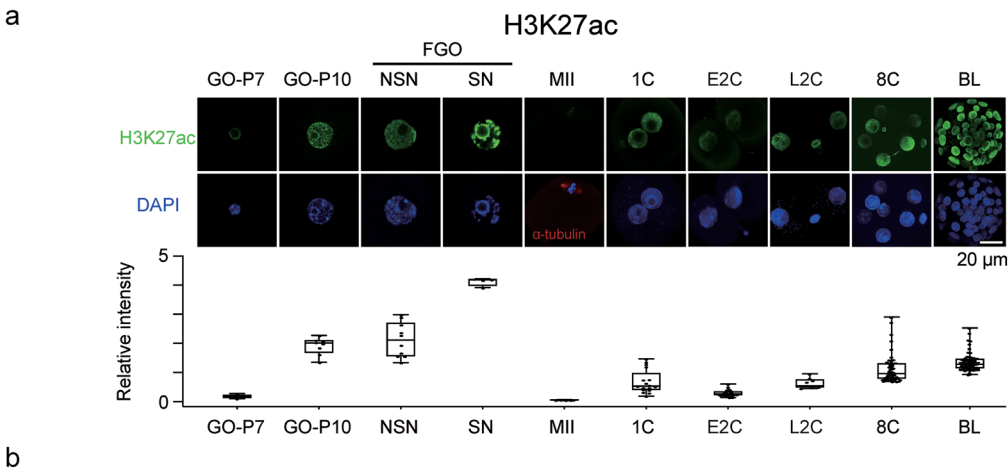
Extended data is available for this paper at https://doi.org/10.1038/s41556-024-01422-x.

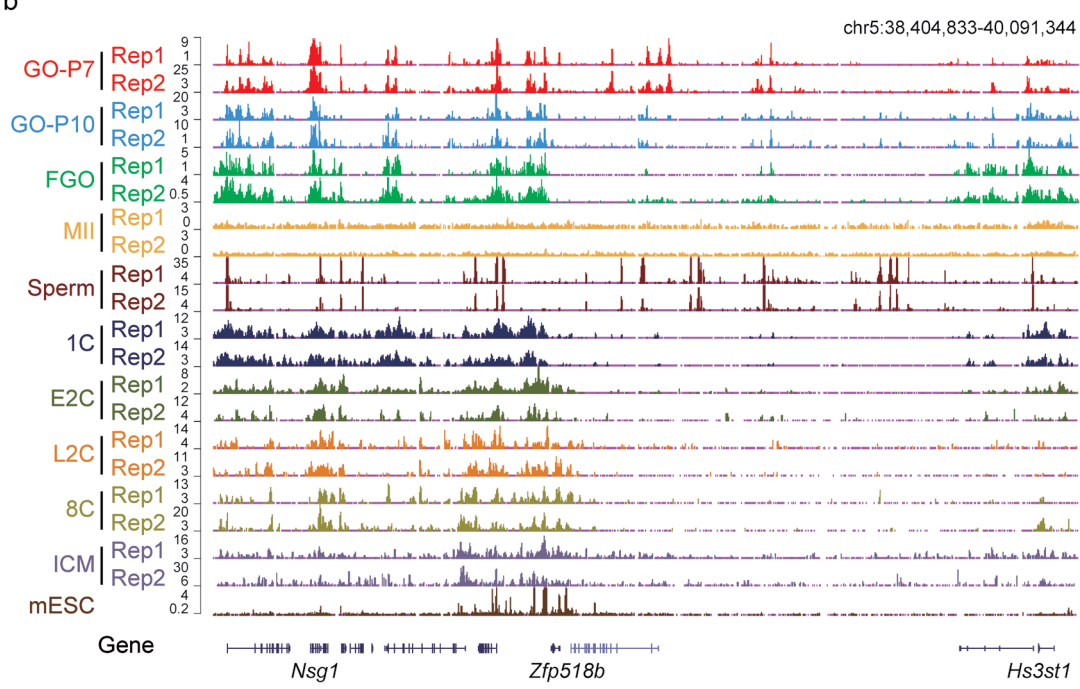
Supplementary information The online version contains supplementary material available at https://doi.org/10.1038/s41556-024-01422-x.

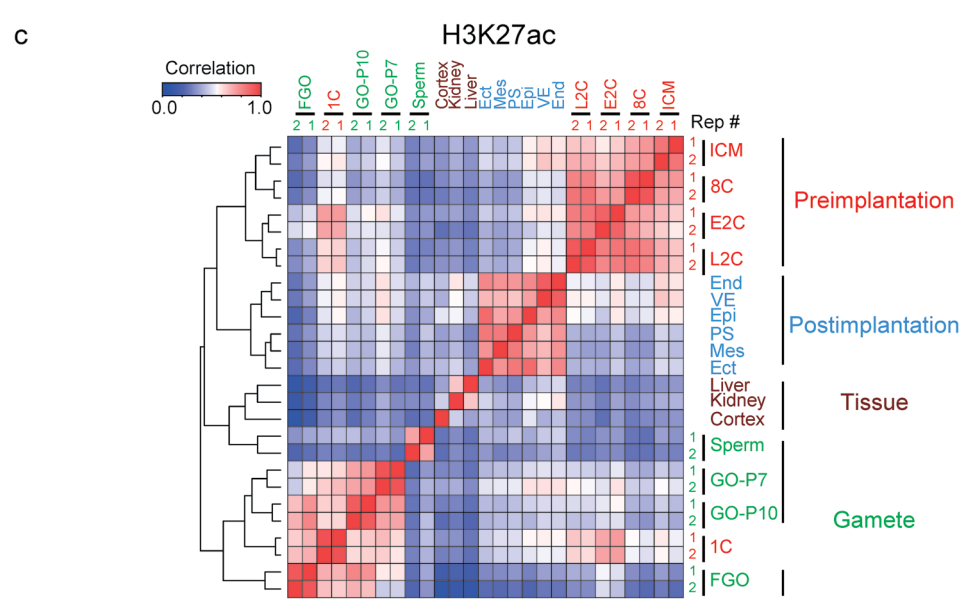
Correspondence and requests for materials should be addressed to Jing Li or Wei Xie.

Peer review information *Nature Cell Biology* thanks Chih-Jen Lin and the other, anonymous, reviewer(s) for their contribution to the peer review of this work.

Reprints and permissions information is available at www.nature.com/reprints.



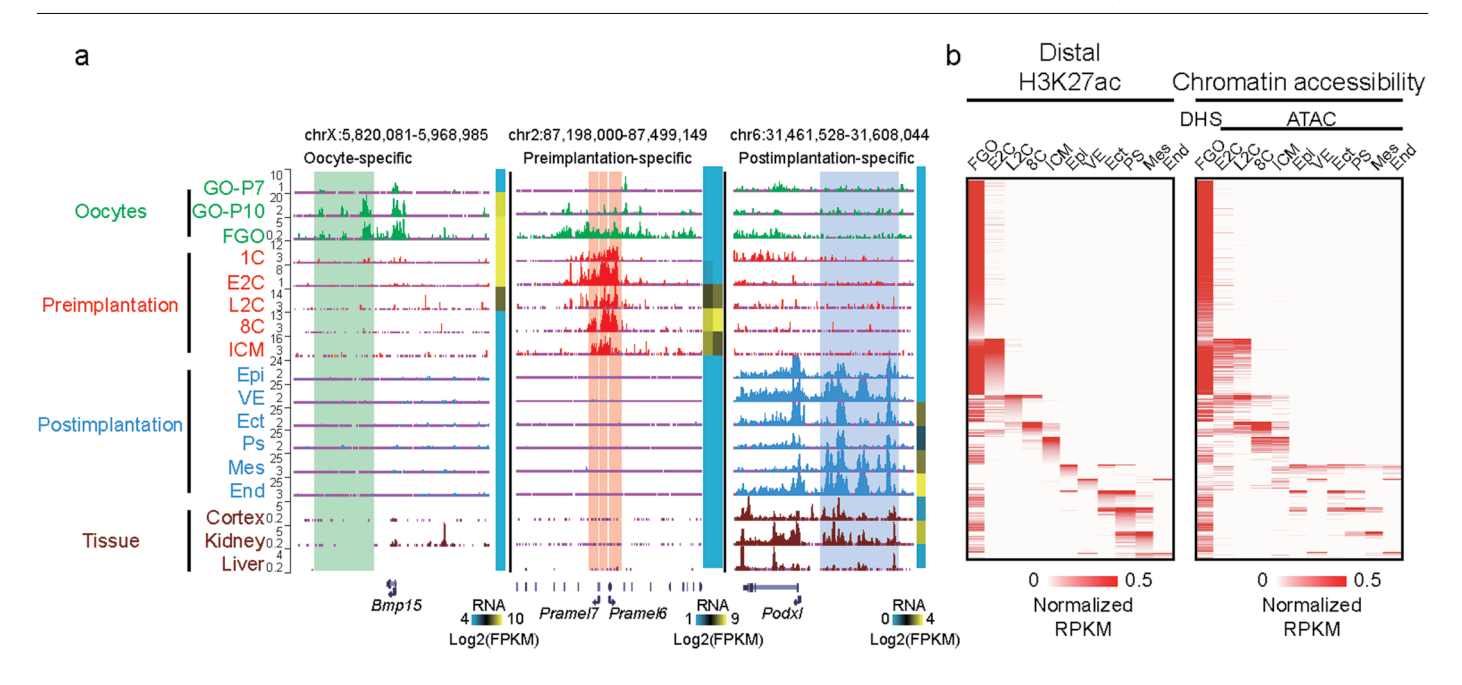


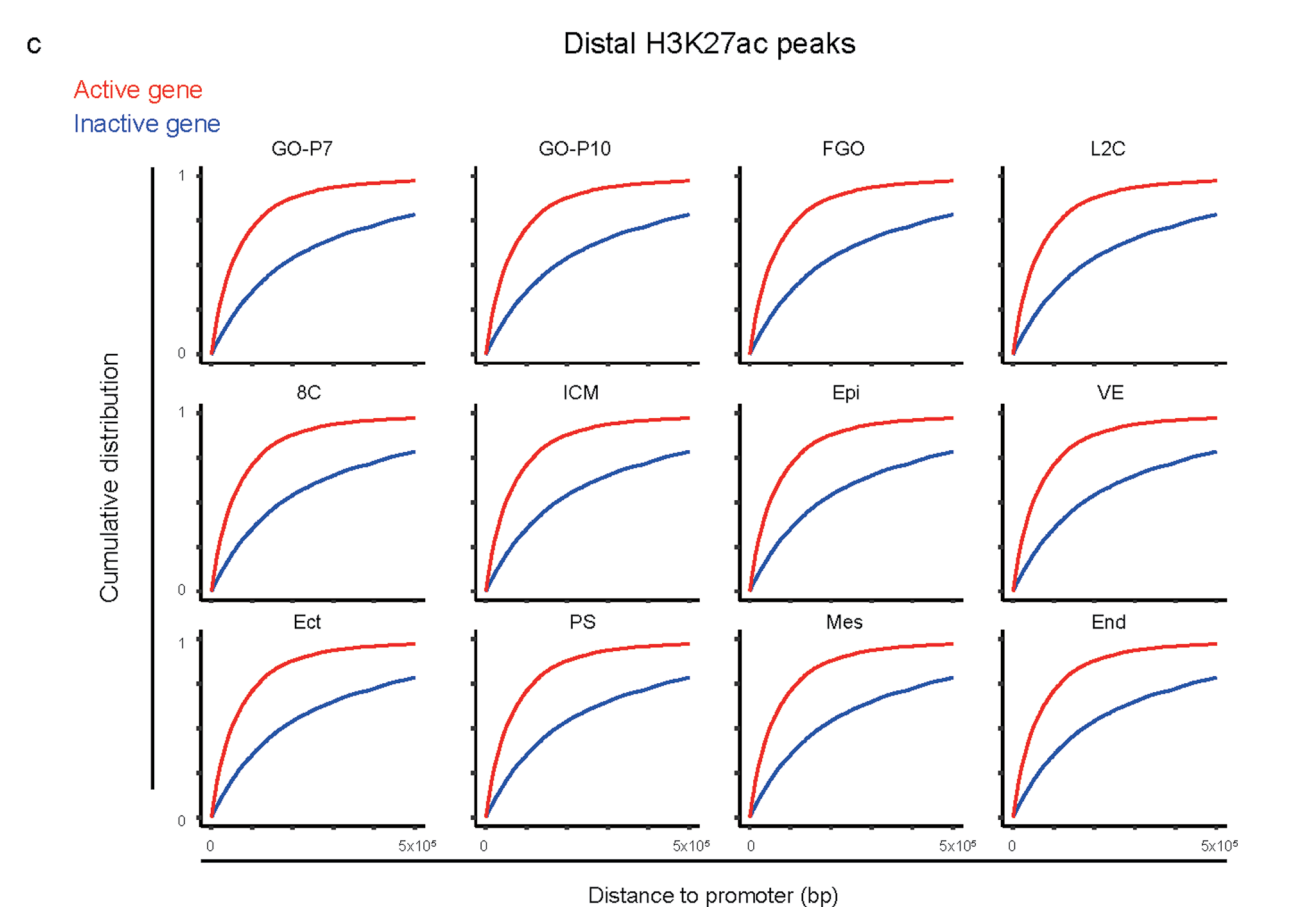


Extended Data Fig. 1 | See next page for caption.

Extended Data Fig. 1 | Validation of H3K27ac ChIP-seq data in mouse oocytes and early embryos. a, Top, immunostaining showing H3K27ac signals in GO-P7 (n=9), GO-P10 (n=8), FGO-NSN (non-surrounded nucleolus) (n=10), FGO-SN (surrounded nucleolus) (n=4), MII oocyte (n=8), one-cell PN5 (n=16), early two-cell (n=19), late two-cell (n=9), 8-cell embryos (n=6), and blastocyst (n=5). One representative image from 3 independent experiments is shown. Scale bar, 20 μ m. Bottom, boxplot showing the ratio of H3K27ac to DAPI intensity

in immunostaining. The median is indicated by the center line. The bottom, top edges, and whiskers represent the 10th and 90th percentiles and 1.5 times the interquartile range (IQR), respectively. **b**, The UCSC browser view showing H3K27ac signals at each stage with two biological replicates. **c**, Heatmap showing the pairwise Pearson correlation between each sample for their H3K27ac levels in oocytes, early embryos, and tissues. Source numerical data and unprocessed blots are available in source data.

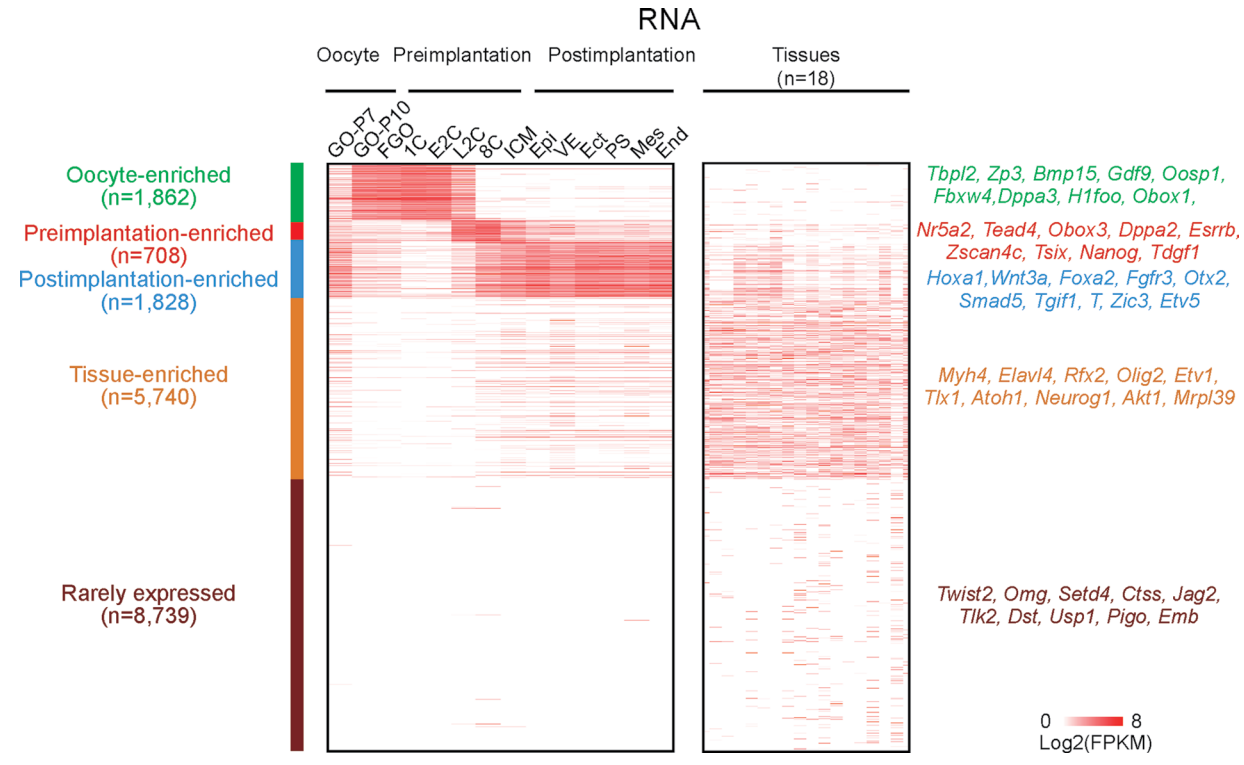




Extended Data Fig. 2 | **H3K27ac, gene expression, and chromatin accessibility in mouse oocytes and early embryos. a**, The UCSC browser view and heatmaps showing H3K27ac signals and RNA expression at representative genes. Oocyte-, pre-implantation- and post-implantation-specific putative enhancers are shaded

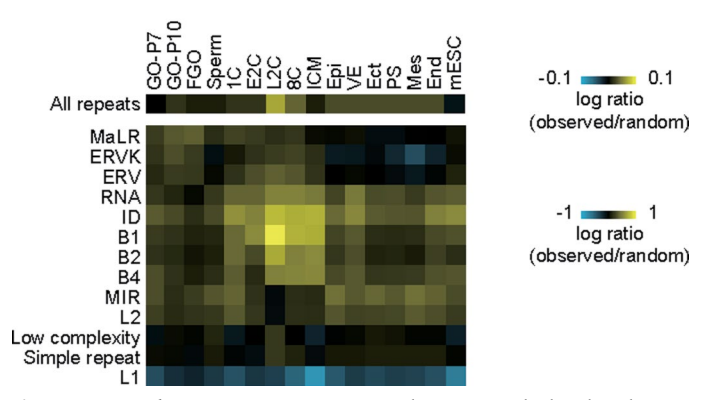
green, red, and blue, respectively. ${f b}$, Heatmaps showing the stage-specific distal

H3K27ac signals and the mapped chromatin accessibility signals. DHS, DNase I hypersensitive site. \mathbf{c} , Line charts showing the cumulative distribution of the distances between promoters of active and inactive genes (top 5,000) and nearest distal H3K27ac sites (top 10,000).



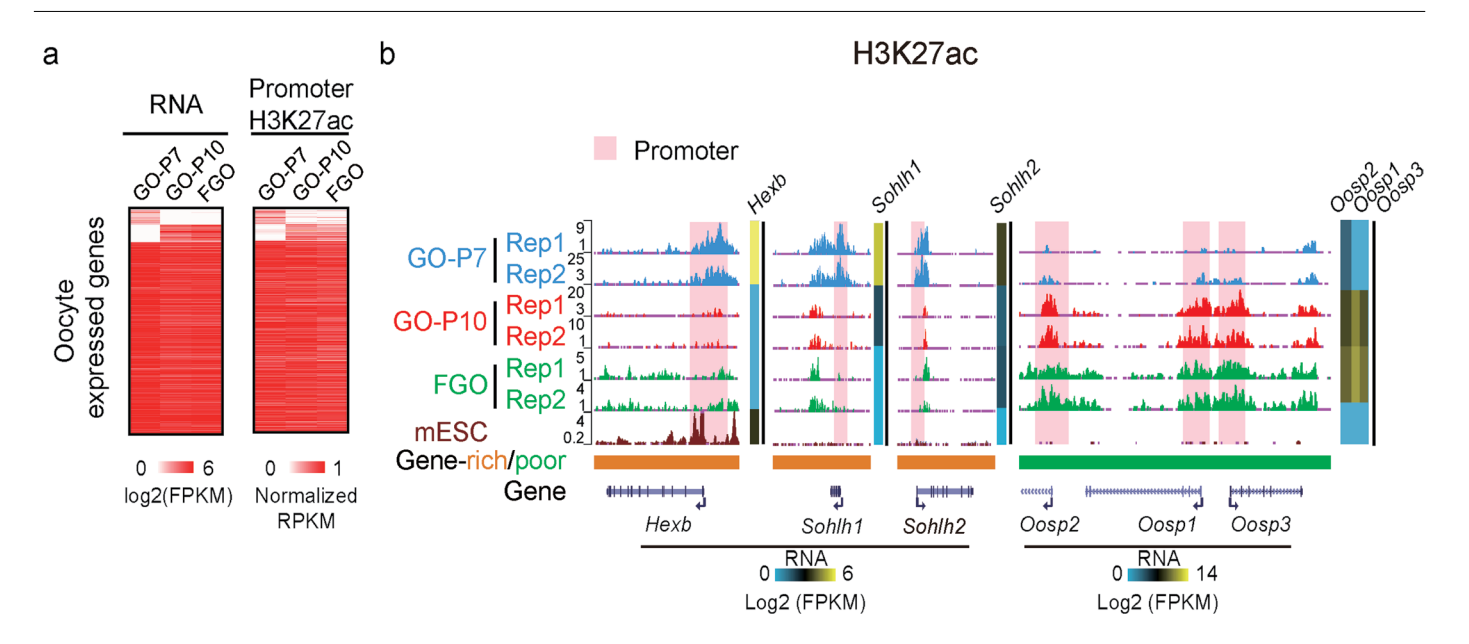
 $\textbf{Extended Data Fig. 3} | \textbf{Gene expression in mouse oocytes, early embryos, and tissues.} \ Heatmaps showing the stage-enriched gene expression in mouse oocytes and early embryos. Mouse adult tissue gene expression <math>9^{7}$ is also mapped. Example genes are listed on the right.

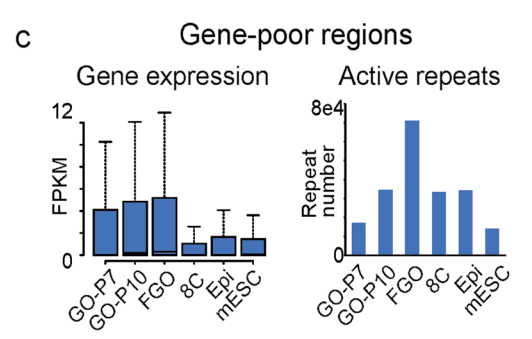
Enrichment of repeats in distal H3K27ac peaks



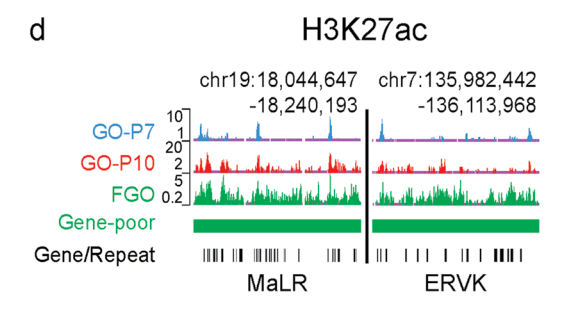
Extended Data Fig. 4 | **Repeat enrichment in H3K27ac peaks.** Heatmaps showing enrichment of all repeat subfamilies at distal H3K27ac peaks compared to that in random peaks in oocytes, early embryos, and mESCs. The H3K27ac

enrichment was calculated as a log2 ratio for the numbers of observed peaks overlapped with repeats divided by those for random peaks (shuffled peaks with lengths matched).

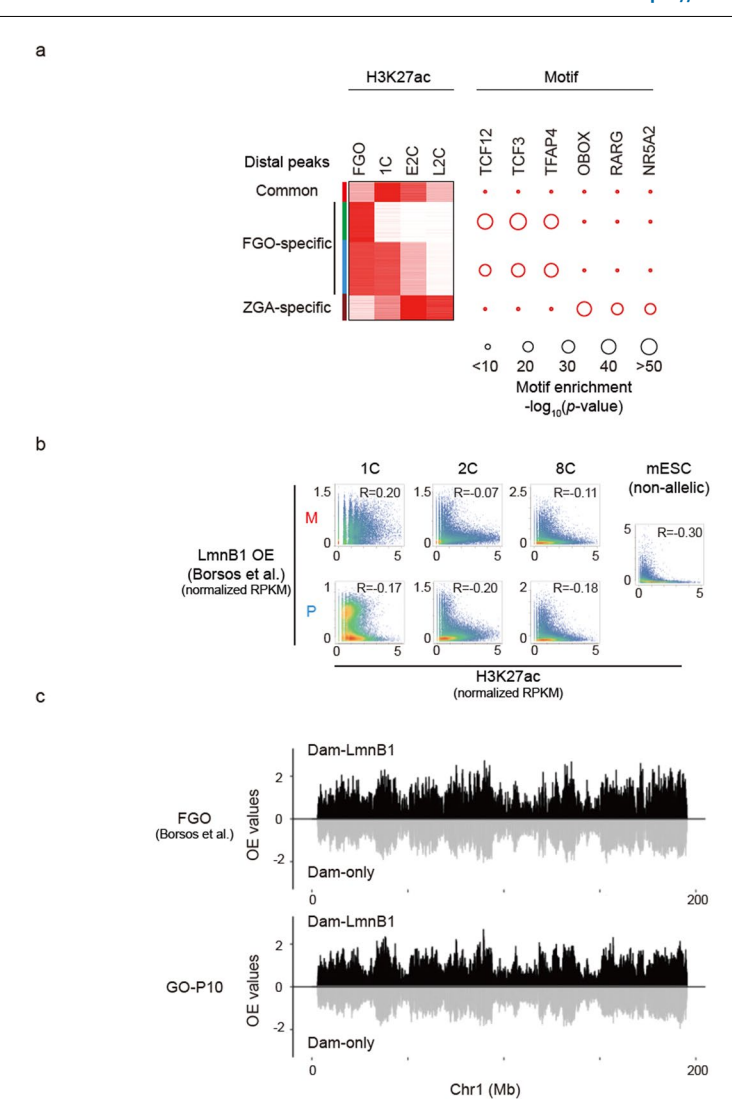




Extended Data Fig. 5 | Dynamics of putative enhancers during mouse oogenesis. a, Heatmaps showing the expression for oocyte stage-specific and common genes with promoter H3K27ac signals mapped. **b**, The UCSC browser views and heatmaps showing H3K27ac signals and RNA expression, respectively, in GO-P7, GO-P10, FGO, and mESCs (ENCODE) with replicates at representative

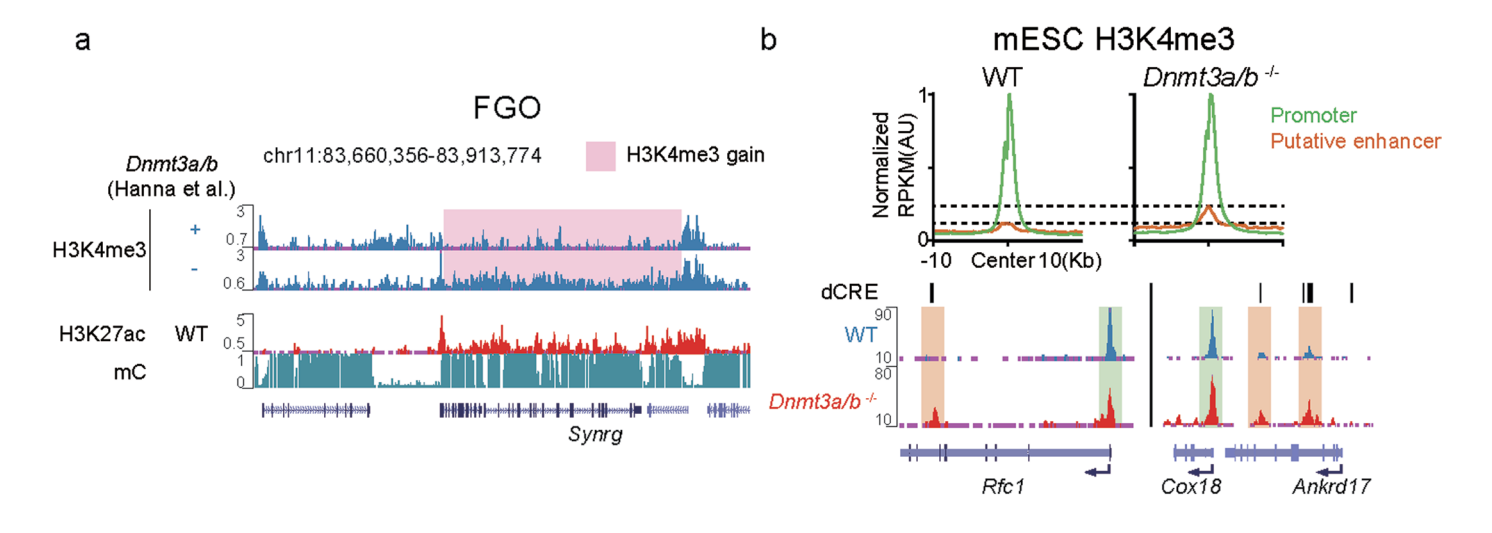


genes. **c**, Bar charts showing the expression levels of genes (left, n=5,505) and the numbers of active repeats (right; GO-P7, n=17,082; GO-P10, n=34,430; FGO, n=70,975; 8C, n=33,384; Epi, n=34,265; mESC, n=14,026) in gene-poor regions at each stage. **d**, The UCSC browser views showing H3K27ac signals at representative repeats in gene-poor regions in GO-P7, GO-P10, and FGOs.



Extended Data Fig. 6 | **The transition of putative enhancers during fertilization and ZGA. a**, Heatmap and bubble plot comparing distal H3K27ac signals and motif enrichment (-log10 p-value, hypergeometric test with Bonferroni correction, one-sided from HOMER 57 , Methods), respectively, at putative enhancers in FGO, one-cell, early two-cell, and late two-cell stage

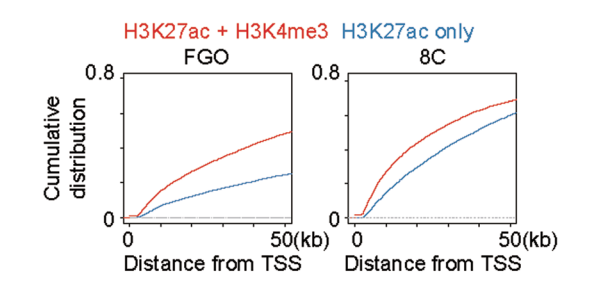
embryos. **b**, Scatter plots comparing allelic H3K27ac and Lamin B1 DamID signals 22 in the one-cell, late two-cell, 8-cell embryos, and mESCs. M, maternal. P, paternal. Pearson correlations of each stage are also shown. **c**, Lamin B1 DamID and DamID-only control signal profiles in FGOs 22 and GO-P10 for chromosome 1 (n=4 biological replicates).



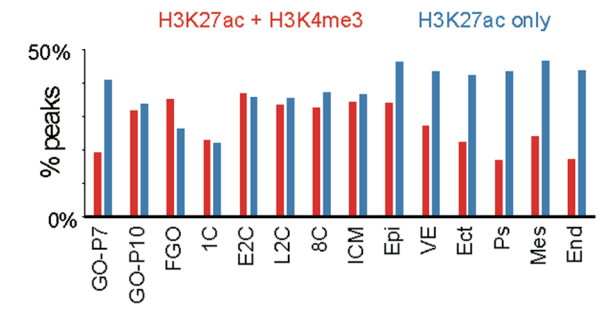
c % Enhancer bound by Pol II

H3K27ac + H3K4me3 H3K27ac only

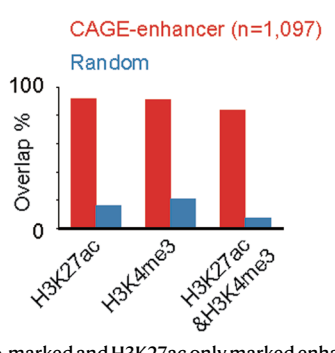
d Enhancer distance to active TSS



e Peaks overlap with distal CREs

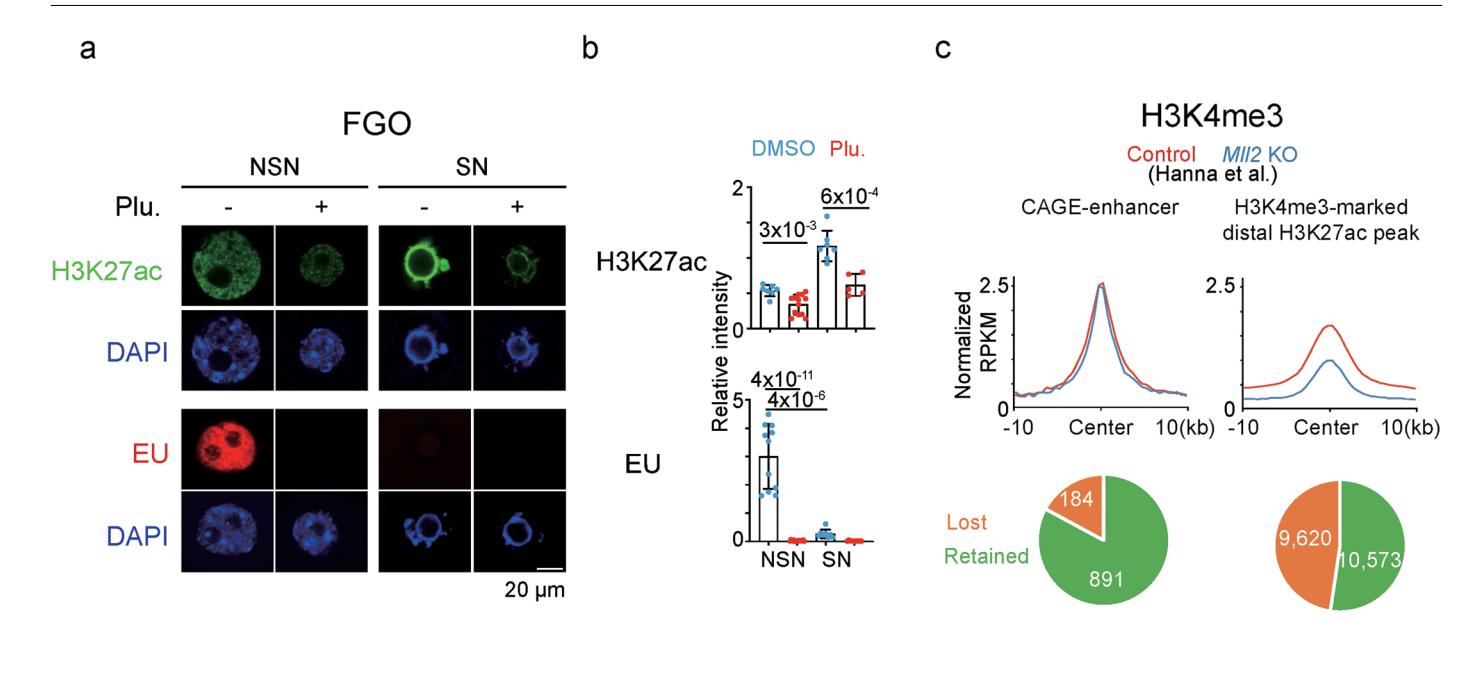


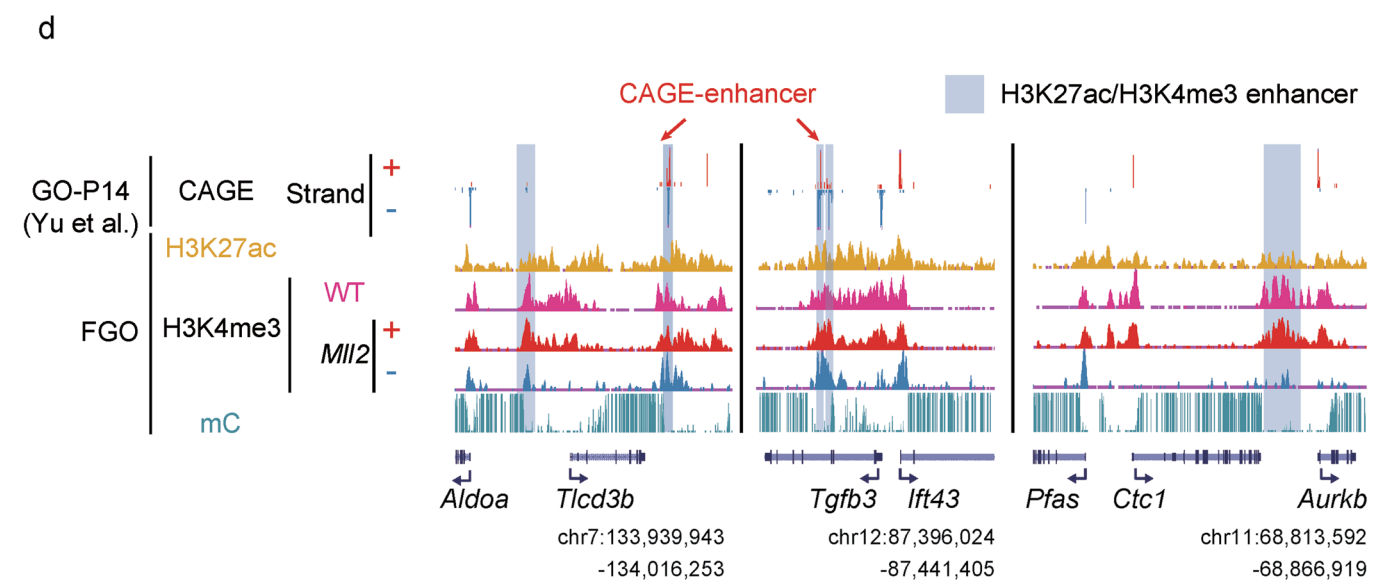
f



Extended Data Fig. 7 | **Analyses of H3K4me3-marked enhancers in oocytes and embryos. a**, The UCSC browser view showing H3K4me3 signals in control and *Dnmt3a/b* knockout FGOs⁴⁰, and H3K27ac and DNA methylation signals in wild-type FGOs. H3K4me3-gain regions upon *Dnmt3a/b* knockout are shaded. **b**, Top, line charts showing H3K4me3 signals at putative enhancers (orange) and promoters (green) in wild-type (left) and *Dnmt3a/b* KO (right) mESCs. The dashed lines indicate the peaks of H3K4me3 signals at putative enhancer regions. Bottom, the UCSC browser views showing H3K4me3 signals at promoters and putative enhancers (annotated ENCODE dCRE) at representative genes in wild-type and *Dnmt3a/b* KO mESCs. Putative enhancer and promoter regions are shaded orange and green, respectively. **c**, Bar chart showing the percentages of

 $\rm H3K27ac/H3K4me3$ co-marked and H3K27ac only marked enhancers bound by distal Pol II 34 at each stage. $\bf d$, Line charts showing the cumulative distribution of the distance between transcription start sites (TSSs) of active gene and nearest distal putative enhancers marked by either H3K27ac only (blue) or both H3K27ac and H3K4me3 (red) in FGO (left) and the 8-cell embryos (right). $\bf e$, Bar chart showing the percentages of H3K27ac only (blue) and H3K27ac/H3K4me3 (red) peaks that also overlap ENCODE dCREs. $\bf f$, Bar chart showing the percentages of CAGE-defined enhancer sites that also overlap H3K27ac sites, H3K4me3 sites, or both. Random sites with identical lengths and numbers were similarly analysed as controls.

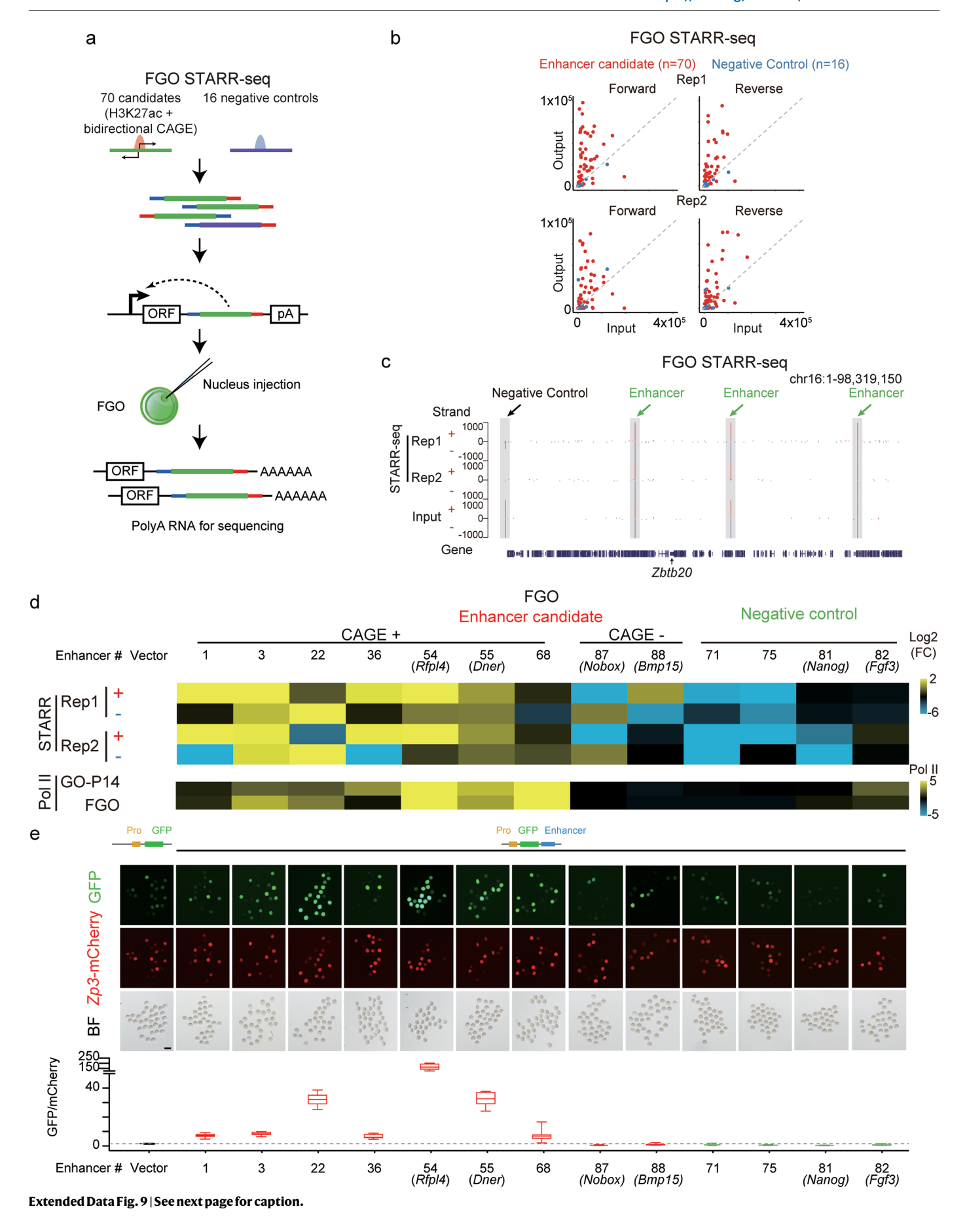




Extended Data Fig. 8 | Analyses of enhancer activities in oocytes.

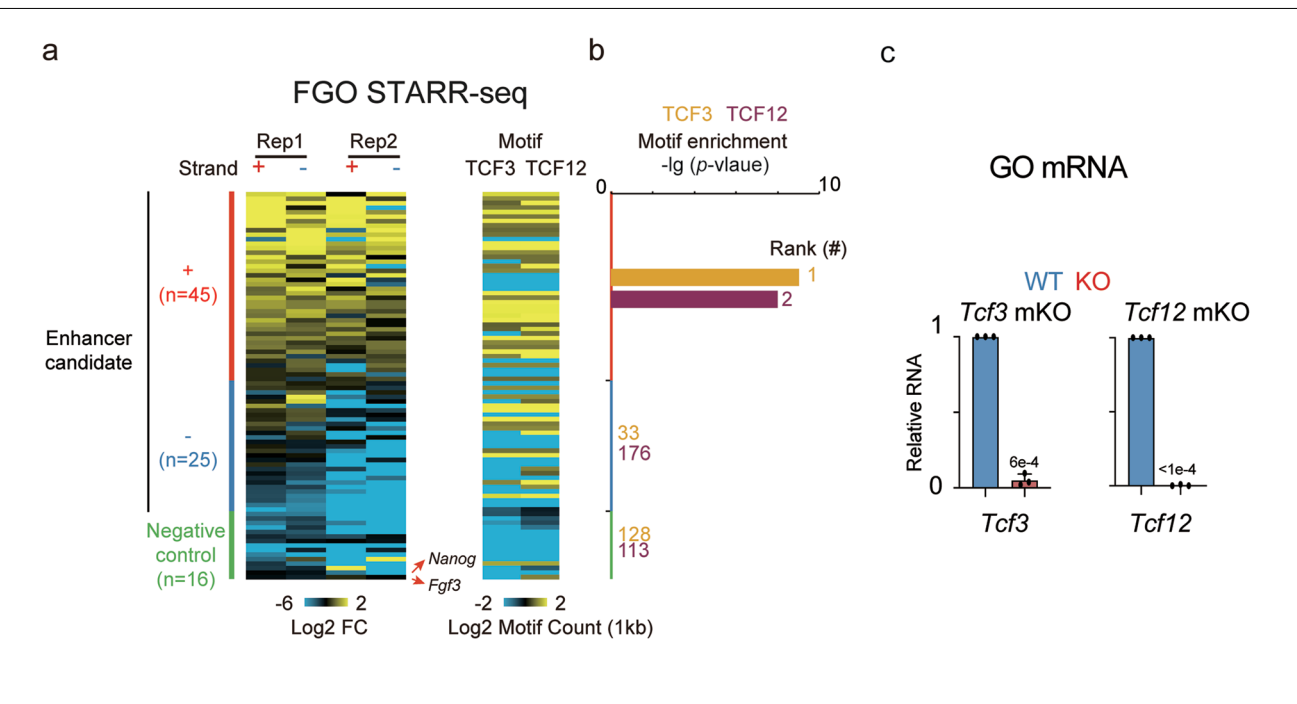
a, Representative images of H3K27ac immunostaining (green) and EU staining (red) in DMSO or plumbagin-treated FGO-NSN and FGO-SN. DNA was stained with DAPI (blue). Scale bar, $20\mu m$. **b**, Bar charts showing the relative intensities of H3K27ac or EU in DMSO (blue) or plumbagin (red) treated FGO-NSN and FGO-SN. The dots indicate the relative intensities of individual oocytes. The numbers of oocytes used: 7, 13, 7, and 5 for H3K27ac (top), and 11, 17, 8, and 9 for EU staining (bottom). *P*-values (*t*-test, two-sided) are also provided. **c**, Line charts showing

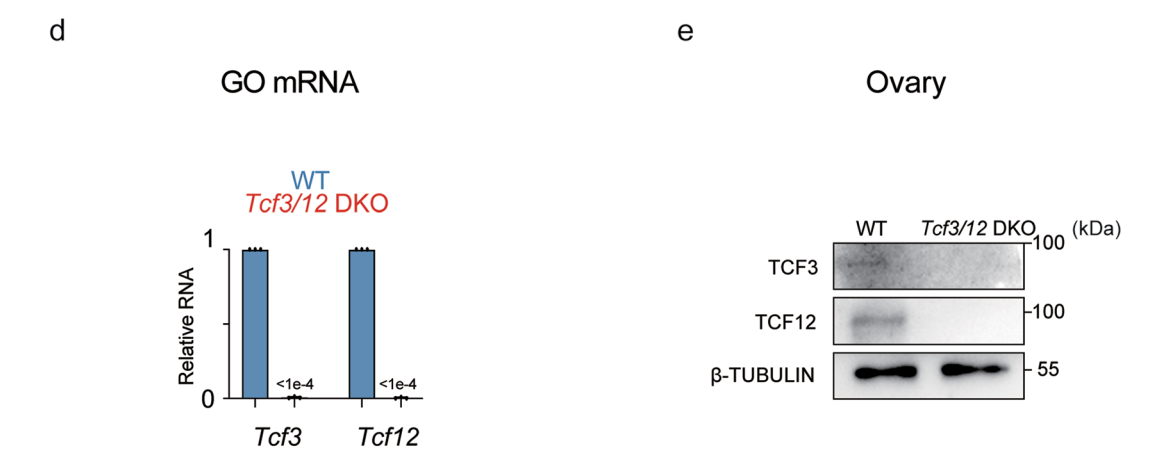
 $\rm H3K4me3\,signals\,at\,CAGE\text{-}enhancers\,and\,H3K4me3\text{-}marked\,distal\,H3K27ac}$ peaks in $\it Mll2\rm\,control\,and\,KO\,oocytes^{40}$. Pie charts showing the percentages of CAGE-enhancers and H3K4me3 at distal H3K27ac peaks in $\it Mll2\rm\,KO\,oocytes$ compared with wild-type. $\it d$. The UCSC browser views showing CAGE in GO-P14 (ref. 46), H3K27ac, and H3K4me3 in FGOs. Putative enhancer regions defined by CAGE (red arrows) or distal H3K27ac (blue shades) are indicated. Source numerical data and unprocessed blots are available in source data.

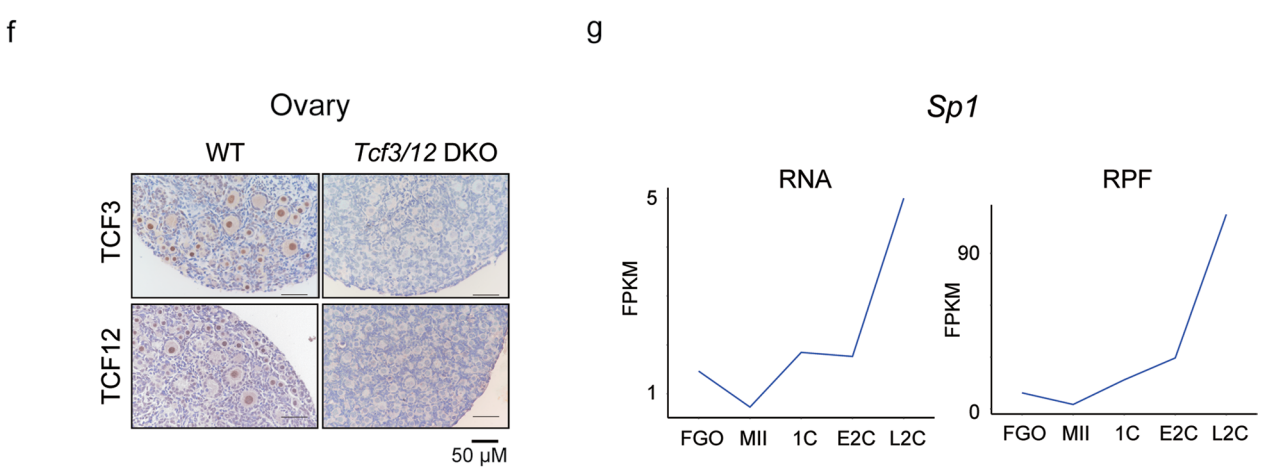


Extended Data Fig. 9 | STARR-seq and reporter assay in oocytes. a, Schematic of STARR-seq in FGOs. 70 candidates and 16 negative controls were manually cloned into the STARR-seq constructs and then the pooled products were injected into the nuclei of FGOs. The RNA was recovered by a method adapted from Smart-seq2 (ref. 54) (Methods) to suit low-input cells, followed by sequencing. **b**, Scatter plots showing STARR-seq signals (RNA output vs. DNA input) (Methods) in both replicates and strands. Red, enhancer candidates; blue, negative control elements. **c**, UCSC genome browser showing FGO STARR-seq RNA output and DNA input signals on chromosome 16. **d**, Heatmaps showing STARR-seq (STARR/input) signals in FGO with two replicates and Pol II signals in

GO-P14 and FGO at enhancer candidates and negative control regions. **e**. Top, fluorescence and bright fields of mouse FGOs in an enhancer reporter assay (Pro, mini promoter). Scale bar, $100 \, \mu m$. Bottom, boxplot showing the ratio of GFP to mCherry intensity in the enhancer reporter assay. The dashed line indicates the ratio in the empty vector group. The numbers of oocytes used in each group: 17,14,17,18,10,18,15,17,13,10,12,19,11, and 6. The median is indicated by the center line. The bottom, top edges, and whiskers represent the 10th and 90th percentiles and 1.5 times the interquartile range (IQR), respectively. Source numerical data and unprocessed blots are available in source data.







Extended Data Fig. 10 | See next page for caption.

Extended Data Fig. 10 | TCF3/12 regulate oocyte transcription and

development. a. Heatmaps showing STARR-seq signals (RNA/DNA input) and TCF3/12 motif densities (counts per kb) for enhancer candidates (including those showing positive and negative STARR-seq signals) and negative controls. **b.** Bar charts showing TCF3/12 motif enrichment (-log10 p-value, hypergeometric test with Bonferroni correction, one-sided from HOMER⁵⁷, Methods) in enhancers previously evaluated by STARR-seq and negative controls. Ranks of TCF3/12 motifs among all motifs are also shown. **c**, qPCR results showing relative RNA levels of Tcf3 and Tcf12 in wild-type and Tcf3 or Tcf12 mKO GO-P5 oocytes (n=3

biological replicates). P-value (t-test, two-sided) is also shown. \mathbf{d} , qPCR results showing relative RNA levels of Tcf3 and Tcf12 in WT and Tcf3/12 DKO GO-P5 oocytes (n=3 biological replicates). P-value (t-test, two-sided) is also shown. \mathbf{e} , Western blot showing protein levels of TCF3 and TCF12 in WT and Tcf3/12 DKO GO-P5 ovaries (n=3 biological replicates). \mathbf{f} , Immunohistochemistry (IHC) showing TCF3 and TCF12 in WT (n=5) and Tcf3/12 DKO (n=5) ovaries. Scale bar, 50 μ m. \mathbf{g} , RNA expression and ribosome-protected fragment (RPF, indicating translation level) levels of Sp1 from FGOs to late two-cell embryos are shown 98 . Source numerical data and unprocessed blots are available in source data.

nature portfolio

Corresponding author(s):	Wei Xie
Last updated by author(s):	Mar 14, 2024

Reporting Summary

Nature Portfolio wishes to improve the reproducibility of the work that we publish. This form provides structure for consistency and transparency in reporting. For further information on Nature Portfolio policies, see our <u>Editorial Policies</u> and the <u>Editorial Policy Checklist</u>.

				•	
< ∙	トつ	+1	ist	т.	\sim
.)	ıa	u	וכו	- 11	

For	all statistical analyses, confirm that the following items are present in the figure legend, table legend, main text, or Methods section.
n/a	Confirmed
	The exact sample size (n) for each experimental group/condition, given as a discrete number and unit of measurement
	A statement on whether measurements were taken from distinct samples or whether the same sample was measured repeatedly
\boxtimes	The statistical test(s) used AND whether they are one- or two-sided Only common tests should be described solely by name; describe more complex techniques in the Methods section.
	A description of all covariates tested
	A description of any assumptions or corrections, such as tests of normality and adjustment for multiple comparisons
	A full description of the statistical parameters including central tendency (e.g. means) or other basic estimates (e.g. regression coefficient) AND variation (e.g. standard deviation) or associated estimates of uncertainty (e.g. confidence intervals)
	For null hypothesis testing, the test statistic (e.g. <i>F</i> , <i>t</i> , <i>r</i>) with confidence intervals, effect sizes, degrees of freedom and <i>P</i> value noted <i>Give P values as exact values whenever suitable.</i>
\times	For Bayesian analysis, information on the choice of priors and Markov chain Monte Carlo settings
X	For hierarchical and complex designs, identification of the appropriate level for tests and full reporting of outcomes
	Estimates of effect sizes (e.g. Cohen's <i>d</i> , Pearson's <i>r</i>), indicating how they were calculated
	Our web collection on <u>statistics for biologists</u> contains articles on many of the points above.

Software and code

Policy information about availability of computer code

Data collection

No custom software was used in this study.

Public datasets (e.g. ENCODE) were retrieved in this study as described and cited in the figure legend section.

Sequencing was performed using Illumina Hi-seq XTen and 2500.

Data analysis

Immunofluorescence data were visualized by ImageJ v1.49.

Sequencing data were analyzed as described in the Methods section. Softwares were also include below:

bowtie2, 2.2.2

tophat2, 2.4.0

cufflinks, 2.2.1

samtools 1.3.1

BSMAP 2.74

HOMER 4.11

BEDTools 2.26.0

 $bedGraphToBigWig\ v4$

Seurat 4.2.1

R 4.2.1

python 2.7.12

TreeView, 1.1.6r4

CAGEr 2.4.0

CAGEfightR 1.18.0

ZEN 3.9

DAVID 6.8, https://david-d.ncifcr

For manuscripts utilizing custom algorithms or software that are central to the research but not yet described in published literature, software must be made available to editors and reviewers. We strongly encourage code deposition in a community repository (e.g. GitHub). See the Nature Portfolio guidelines for submitting code & software for further information.

Data

Policy information about availability of data

All manuscripts must include a data availability statement. This statement should provide the following information, where applicable:

- Accession codes, unique identifiers, or web links for publicly available datasets
- A description of any restrictions on data availability
- For clinical datasets or third party data, please ensure that the statement adheres to our policy

All data have been deposited to GEO with the accession number GSE217970. mm9 genome assembly: https://hgdownload.cse.ucsc.edu/goldenpath/mm9/

Research involving human participants, their data, or biological material

Policy information about studies with <u>human participants or human data</u>. See also policy information about <u>sex, gender (identity/presentation)</u>, <u>and sexual orientation</u> and <u>race</u>, ethnicity and racism.

Reporting on sex and gender	N/A
Reporting on race, ethnicity, or other socially relevant groupings	N/A
Population characteristics	N/A
Recruitment	N/A
Ethics oversight	N/A

Note that full information on the approval of the study protocol must also be provided in the manuscript.

Field-specific reporting

Please select the one below that is the best fit for your research. If you are not sure, read the appropriate sections before making your selection.

igwedge Life sciences $ig[$		Behavioural & social sciences		Ecological,	. evolutionary	& environmenta	l science
-----------------------------	--	-------------------------------	--	-------------	----------------	----------------	-----------

For a reference copy of the document with all sections, see <u>nature.com/documents/nr-reporting-summary-flat.pdf</u>

Life sciences study design

All studies must disclose on these points even when the disclosure is negative.

Sample size

No statistical method was used to pre-determine sample size. Sample sizes for 2 to 3 biological replicates including all oocyte, embryo, and cell line H3K27ac STAR ChIP-seq and ATAC-seq in this study were used according to common practice in the field (Zhang, B., Zheng, H., Huang, B., Li, W., Xiang, Y., Peng, X., Ming, J., Wu, X., Zhang, Y., Xu, Q., et al. (2016). Allelic reprogramming of the histone modification H3K4me3 in early mammalian development. Nature 537, 553–557; Wu, J., Huang, B., Chen, H., Yin, Q., Liu, Y., Xiang, Y., Zhang, B., Liu, B., Wang, Q., Xia, W., et al. (2016). The landscape of accessible chromatin in mammalian preimplantation embryos. Nature 534, 652-657).

Data exclusions

During ChIP-seq and ATAC-seq data processing, multiple mapped reads and duplicate reads were removed from downstream analysis.

Replication

Immunofluorescence, western blot, and Immunoprecipitation were preformed 2 to 3 times, and similar observation was made for each replicate. One representative result was shown in the figures.

Replication of sequencing data was confirmed by calculating correlation and reproducibility between replicates (2 to 3 biological replicates), as shown in each figure and figure legend (Fig. S1B-C, Fig. S9B-C).

Randomization

Experimental materials were not divided into random subgroups. Most comparisons were done between WT and mutants.

Blinding

The authors were not blinded to group allocation during sample collection or analysis, as the information on genotype of materials was essential for the experiment design and analysis.

Reporting for specific materials, systems and methods

We require information from authors about some types of materials, experimental systems and methods used in many studies. Here, indicate whether each material, system or method listed is relevant to your study. If you are not sure if a list item applies to your research, read the appropriate section before selecting a response.

Materials & experimental systems	Methods
n/a Involved in the study	n/a Involved in the study
Antibodies	ChIP-seq
Eukaryotic cell lines	Flow cytometry
Palaeontology and archaeology	MRI-based neuroimaging
Animals and other organisms	•
Clinical data	
Dual use research of concern	
·	

Antibodies

Antibodies used

H3K27ac (Active Motif, 39133, 1:200 diluted for immunofluorescent and 1:70 diluted for STAR-ChIP):https://www.activemotif.com/catalog/details/39133/histone-h3-acetyl-lys27-antibody-pab

H3K4me3 (in-house, 1:70 diluted): Zhang, B., Zheng, H., Huang, B., Li, W., Xiang, Y., Peng, X., Ming, J., Wu, X., Zhang, Y., Xu, Q., et al. (2016). Allelic reprogramming of the histone modification H3K4me3 in early mammalian development. Nature 537, 553–557. TCF3 (Proteintech, 21242-1-AP, 1:800 diluted for western blot, 1:200 for IHC, 1:2,000 for IF) https://www.ptglab.com/products/TCF3-Antibody-21242-1-AP.htm

TCF12 (Proteintech, 14419-1-AP, 1:800 diluted for western blot, 1:200 for IHC, 1:2000 for IF): https://www.ptglab.com/products/TCF12-Antibody-14419-1-AP.htm

Alexa Fluor 488 conjugated anti-rabbit (Jackson ImmunoResearch, 611-545-215, 1:200 diluted): https://www.jacksonimmuno.com/catalog/products/611-545-215

LHX8 (Abclonal A2046, 1:2000 for IF): https://abclonal.com/catalog-antibodies/LHX8PolyclonalAntibody/A2046 β -TUBULIN (YIFEIXUE BIOTECH, YFMA0053, 1:1,000 for western blot): http://www.yfxbio.com/product/5221.html

Validation

H3K4me3 for ChIP-seq: Allelic reprogramming of the histone modification H3K4me3 in early mammalian development. Nature 537, 553–557.

H3K27ac for ChIP-seq and IF: https://www.activemotif.com/catalog/details/39133/histone-h3-acetyl-lys27-antibody-pab

Western blot and IF for TCF3: https://www.ptglab.com/products/TCF3-Antibody-21242-1-AP.htm

Western blot and IF for TCF12: https://www.ptglab.com/products/TCF12-Antibody-14419-1-AP.htm

 $IF for Alexa \ Fluor \ 488 \ conjugated \ anti-rabbit: https://www.jacksonimmuno.com/catalog/products/611-545-215$

IF for LHX8: https://abclonal.com/catalog-antibodies/LHX8PolyclonalAntibody/A2046

Western blot for β-TUBULIN: http://www.yfxbio.com/product/5221.html

Eukaryotic cell lines

Policy information about cell lines and Sex and Gender in Research

Cell line source(s)

Muthentication

Pluripotency and naïve markers were expressed in our mouse mES cells validated by smart-seq. Gene expression in our HEK293T cells was validated by smart-seq and compared with the reference (Zou, Z. et al. Translatome and transcriptome coprofiling reveals a role of TPRXs in human zygotic genome activation. Science 378, abo7923 (2022)).

Mycoplasma contamination

All cell lines tested negative for mycoplasma contamination.

No commonly misidentified cell lines were used in this study.

Commonly misidentified lines (See ICLAC register)

Animals and other research organisms

Policy information about <u>studies involving animals</u>; <u>ARRIVE guidelines</u> recommended for reporting animal research, and <u>Sex and Gender in</u> Research

Laboratory animals

C57/BL6, male and female, 4-8 weeks, from Vital River and Tsinghua Animal Center; PWK/PhJ, from Jackson Laboratory.

Tcf3flox/flox and Tcf12flox/flox transgenic mice were gifted from Prof. Yuan Zhuang at Duke University. Gdf9-Cre mice were gifted from Prof. Youqiang Su at Shandong University.

All mice were housed in a Specific Pathogen Free (SPF) facility with individually ventilated cages. The room has controlled temperature (20-22°C), humidity (30%–70%) and light (12 hour light-dark cycle). Mice were provided ad libitum access to a regular rodent chow diet.

All animal maintenance and experimental procedures used in current study were carried out according to guidelines of Institutional

	Animal Care and Use Committee (IACUC) of Tsinghua University, Beijing, China.
Wild animals	The study did not involve wild animals
Reporting on sex	All the embryos and oocytes were collected from female mice.
Field-collected samples	No field-collected samples were used in this study.
Ethics oversight	All animal maintenance and experimental procedures used in current study were carried out according to guidelines of Institutional Animal Care and Use Committee (IACUC) of Tsinghua University, Beijing, China.

Note that full information on the approval of the study protocol must also be provided in the manuscript.

Plants

Seed stocks	N/A
Novel plant genotypes	N/A
Authentication	N/A

ChIP-seq

Data deposition

Confirm that both raw and final processed data have been deposited in a public database such as GEO.

Confirm that you have deposited or provided access to graph files (e.g. BED files) for the called peaks.

FGO_STARR_seq_rep2

Data access links

May remain private before publication.

All data have been deposited to GEO with the accession number GSE217970.

Files in database submission

```
All the data information were included in GEO accession GSE217970 and Methods part.
2cell_early_H3K27ac_rep1
2cell_early_H3K27ac_rep2
2cell_late_H3K27ac_rep1
2cell_late_H3K27ac_rep2
2cell_late_Parthenogenetic_Eed_control_H3K27ac_rep1
2cell_late_Parthenogenetic_Eed_control_H3K27ac_rep2
2cell_late_Parthenogenetic_Eed_KO_H3K27ac_rep1
2cell_late_Parthenogenetic_Eed_KO_H3K27ac_rep2
8cell_H3K27ac_rep1
8cell_H3K27ac_rep2
FGO H3K27ac rep1
FGO_H3K27ac_rep2
GO_P10_H3K27ac_rep1
GO_P10_H3K27ac_rep2
GO_P7_H3K27ac_rep1
GO P7 H3K27ac rep2
ICM_H3K27ac_rep1
ICM_H3K27ac_rep2
mESC_Dnmt3ab_dKO_H3K4me3_rep1
mESC_Dnmt3ab_dKO_H3K4me3_rep2
mESC_Dnmt3ab_Setd2_tKO_H3K4me3_rep1
mESC Dnmt3ab Setd2 tKO H3K4me3 rep2
mESC_WT_H3K4me3_rep1
mESC_WT_H3K4me3_rep2
mESC_H3K27ac_500_rep1
mESC_H3K27ac_500_rep2
MII H3K27ac rep1
MII_H3K27ac_rep2
PN5_H3K27ac_rep1
PN5_H3K27ac_rep2
sperm_H3K27ac_rep1
sperm_H3K27ac_rep2
FGO_STARR_seq_rep1
```

```
STARR lib DNA input
p10_Dam_1
p10_Dam_2
p10_Dam_3
p10_Dam_4
p10 Lamin 1
p10_Lamin_2
p10_Lamin_3
p10_Lamin_4
C-10_A_control_primodial_single_oocyte_RNA
C-16 A control primodial single oocyte RNA
C-17_A_control_primodial_single_oocyte_RNA
C-18_A_control_primodial_single_oocyte_RNA
C-19_A_control_primodial_single_oocyte_RNA
C-1\_A\_control\_primodial\_single\_oocyte\_RNA
C-20\_A\_control\_primodial\_single\_oocyte\_RNA
C-22_A_control_primodial_single_oocyte_RNA
C-23_A_control_primodial_single_oocyte_RNA
C-28_B_control_primary_single_oocyte_RNA
C-29 B control primary single oocyte RNA
C-30_B_control_primary_single_oocyte_RNA
C-31\_B\_control\_primary\_single\_oocyte\_RNA
C-32_B_control_primary_single_oocyte_RNA
C-33_B_control_primary_single_oocyte_RNA
C-34_B_control_primary_single_oocyte_RNA
C-35_B_control_primary_single_oocyte_RNA
C-36\_B\_control\_primary\_single\_oocyte\_RNA
C-37 B control primary single oocyte RNA
C-38_B_control_primary_single_oocyte_RNA
C\text{-}39\_B\_control\_primary\_single\_oocyte\_RNA
C-3 A control primodial single oocyte RNA
C-44_B_control_primary_single_oocyte_RNA
C-45_B_control_primary_single_oocyte_RNA
C-46_B_control_primary_single_oocyte_RNA
\hbox{C-47\_B\_control\_primary\_single\_oocyte\_RNA}
C-48 B control primary single oocyte RNA
C-49\_B\_control\_primary\_single\_oocyte\_RNA
C-50\_B\_control\_primary\_single\_oocyte\_RNA
C-51 B control primary single oocyte RNA
C-52_C_control_secondary_single_oocyte_RNA
C-53_C_control_secondary_single_oocyte_RNA
C-54_C_control_secondary_single_oocyte_RNA
C-55_C_control_secondary_single_oocyte_RNA
C-5 A control primodial_single_oocyte_RNA
C-65_C_control_secondary_single_oocyte_RNA
C-66_C_control_secondary_single_oocyte_RNA
C-67_C_control_secondary_single_oocyte_RNA
C-68_C_control_secondary_single_oocyte_RNA
C-69\_C\_control\_secondary\_single\_oocyte\_RNA
C-6 A control primodial single oocyte RNA
C-70_C_control_secondary_single_oocyte_RNA
C-71\_C\_control\_secondary\_single\_oocyte\_RNA
C-72_C_control_secondary_single_oocyte_RNA
C-73_C_control_secondary_single_oocyte_RNA
C-74\_C\_control\_secondary\_single\_oocyte\_RNA
C-75 C control secondary single oocyte RNA
C-76_C_control_secondary_single_oocyte_RNA
C-7_A_control_primodial_single_oocyte_RNA
C-85_C_control_secondary_single_oocyte_RNA
C-86\_C\_control\_secondary\_single\_oocyte\_RNA
C-87_C_control_secondary_single_oocyte_RNA
C-88_C_control_secondary_single_oocyte_RNA
C-89_C_control_secondary_single_oocyte_RNA
C-8_A_control_primodial_single_oocyte_RNA
C-90_D_control_secondary_single_oocyte_RNA
C-91_D_control_secondary_single_oocyte_RNA
C-92_D_control_secondary_single_oocyte_RNA
C-9_A_control_primodial_single_oocyte_RNA
T-10 a Tcf3 12 dKO primodial single oocyte RNA
T-1_a_Tcf3_12_dKO_primodial_single_oocyte_RNA
T-26\_a\_Tcf3\_12\_dKO\_primodial\_single\_oocyte\_RNA
T-27_a_Tcf3_12_dKO_primodial_single_oocyte_RNA
T-28\_a\_Tcf3\_12\_dKO\_primodial\_single\_oocyte\_RNA
T-29_a_Tcf3_12_dKO_primodial_single_oocyte_RNA
T-2 a Tcf3 12 dKO primodial single oocyte RNA
T-30_a_Tcf3_12_dKO_primodial_single_oocyte_RNA
```

```
T-31 a Tcf3 12 dKO primodial single oocyte RNA
T-32_a_Tcf3_12_dKO_primodial_single_oocyte_RNA
T-33_b_Tcf3_12_dKO_primary_single_oocyte_RNA
T-34_b_Tcf3_12_dKO_primary_single_oocyte_RNA
T\text{-}35\_b\_Tcf3\_12\_dKO\_primary\_single\_oocyte\_RNA
T-36_b_Tcf3_12_dKO_primary_single_oocyte_RNA
T-37_b_Tcf3_12_dKO_primary_single_oocyte_RNA
T\text{-}38\_b\_Tcf3\_12\_dKO\_primary\_single\_oocyte\_RNA
T-39 b Tcf3 12 dKO primary single oocyte RNA
T-3_a_Tcf3_12_dKO_primodial_single_oocyte_RNA
T-40\_b\_Tcf3\_12\_dKO\_primary\_single\_oocyte\_RNA
T-41_b_Tcf3_12_dKO_primary_single_oocyte_RNA
T-42_b_Tcf3_12_dKO_primary_single_oocyte_RNA
T-43_b_Tcf3_12_dKO_primary_single_oocyte_RNA
T-44_b_Tcf3_12_dKO_primary_single_oocyte_RNA
T-45\_b\_Tcf3\_12\_dKO\_primary\_single\_oocyte\_RNA
T-46_b_Tcf3_12_dKO_primary_single_oocyte_RNA
T-47_b_Tcf3_12_dKO_primary_single_oocyte_RNA
T-48\_b\_Tcf3\_12\_dKO\_primary\_single\_oocyte\_RNA
T-49 b Tcf3 12 dKO primary single oocyte RNA
T-4_a_Tcf3_12_dKO_primodial_single_oocyte_RNA
T-50\_b\_Tcf3\_12\_dKO\_primary\_single\_oocyte\_RNA
T-51_b_Tcf3_12_dKO_primary_single_oocyte_RNA
T-52_b_Tcf3_12_dKO_primary_single_oocyte_RNA
T-53_b_Tcf3_12_dKO_primary_single_oocyte_RNA
T-54_b_Tcf3_12_dKO_primary_single_oocyte_RNA
T-55\_b\_Tcf3\_12\_dKO\_primary\_single\_oocyte\_RNA
T-56_b_Tcf3_12_dKO_primary_single_oocyte_RNA
T-57_b_Tcf3_12_dKO_primary_single_oocyte_RNA
T-58\_b\_Tcf3\_12\_dKO\_primary\_single\_oocyte\_RNA
T-5 a Tcf3 12 dKO primodial single oocyte RNA
T-66_b_Tcf3_12_dKO_primary_single_oocyte_RNA
T-67_c_Tcf3_12_dKO_secondary_single_oocyte_RNA
T-68_c_Tcf3_12_dKO_secondary_single_oocyte_RNA
T-69_c_Tcf3_12_dKO_secondary_single_oocyte_RNA
T-6 a Tcf3 12 dKO primodial single oocyte RNA
T-70_c_Tcf3_12_dKO_secondary_single_oocyte_RNA
T-71\_c\_Tcf3\_12\_dKO\_secondary\_single\_oocyte\_RNA
T-72 c Tcf3 12 dKO secondary single oocyte RNA
T-73_c_Tcf3_12_dKO_secondary_single_oocyte_RNA
T-74\_c\_Tcf3\_12\_dKO\_secondary\_single\_oocyte\_RNA
T-75_c_Tcf3_12_dKO_secondary_single_oocyte_RNA
T-76_c_Tcf3_12_dKO_secondary_single_oocyte_RNA
T-77 c Tcf3 12 dKO secondary single oocyte RNA
T-78_c_Tcf3_12_dKO_secondary_single_oocyte_RNA
T-79_c_Tcf3_12_dKO_secondary_single_oocyte_RNA
T-7 a Tcf3 12 dKO primodial single oocyte RNA
T-8 a _Tcf3_12_dKO_primodial_single_oocyte_RNA
T-90_c_Tcf3_12_dKO_secondary_single_oocyte_RNA
T-93 c Tcf3 12 dKO secondary single oocyte RNA
T-95 c Tcf3 12 dKO secondary single oocyte RNA
T-9_a_Tcf3_12_dKO_primodial_single_oocyte_RNA
```

Genome browser session (e.g. <u>UCSC</u>)

The processed BigWig files were included in GEO accession GSE217970

Methodology

Replicates

Sample sizes for 2 to 3 biological replicates including all oocyte, embryo, and cell line H3K27ac STAR ChIP-seq in this study were used according to common practice in the field. The replicates were included in GEO accession GSE217970.

Sequencing depth

Each stage of oocyte and embryo STAR ChIP-seq with pooled more than 15M uniq-mapped reads.

Antibodies

H3K27ac (Active Motif, 39133):https://www.activemotif.com/catalog/details/39133/histone-h3-acetyl-lys27-antibody-pab H3K4me3 (in-house): Zhang, B., Zheng, H., Huang, B., Li, W., Xiang, Y., Peng, X., Ming, J., Wu, X., Zhang, Y., Xu, Q., et al. (2016). Allelic reprogramming of the histone modification H3K4me3 in early mammalian development. Nature 537, 553–557.

Peak calling parameters

Peaks were called by HOMER with the parameters -region -size 1000 -minDist 1500 -gsize 2.9e9 -fdr 0.0005. The peaks with tag count numbers more than 40 were selected as strong peaks for downstream analysis.

Data quality

Data quality was confirmed and validated by calculating correlation and reproducibility between replicates (2 to 3 biological replicates), as shown in each figure and figure legend (Fig. S1B-C, Fig. S9B-C).

Software

Sequencing data were analyzed as described in the Methods section. Softwares were also include below: bowtie2, 2.2.2

samtools 1.3.1 HOMER 4.11 bedtools2 2.26.0 bedGraphToBigWig v4 R 4.2.1 python 2.7.12